

# Casein-Coated Molybdenum Disulfide Nanosheets Augment the Bioactivity of Alginate Microspheres for Orthopedic Applications

Pandurang Appana Dalavi, Ashwini Prabhu, Sajida M, Kaushik Chatterjee, and Jayachandran Venkatesan\*



Cite This: *ACS Omega* 2022, 7, 26092–26106



Read Online

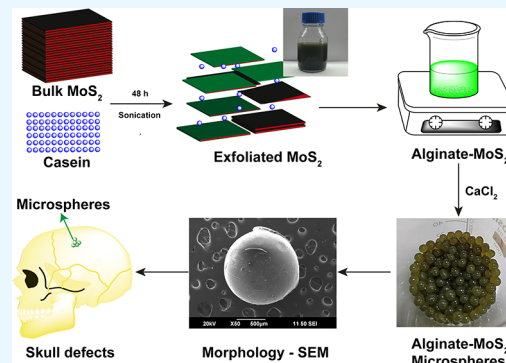
ACCESS |

Metrics & More

Article Recommendations

Supporting Information

**ABSTRACT:** Defects and disorders of the bone due to disease, trauma, or abnormalities substantially affect a person's life quality. Research in bone tissue engineering is motivated to address these clinical needs. The present study demonstrates casein-mediated liquid exfoliation of molybdenum disulfide ( $\text{MoS}_2$ ) and its coupling with alginate to create microspheres to engineer bone graft substitutes. Casein-exfoliated nano- $\text{MoS}_2$  was chemically characterized using different analytical techniques. The UV-visible spectrum of nano- $\text{MoS}_2$ -2 displayed strong absorption peaks at 610 and 668 nm. In addition, the XPS spectra confirmed the presence of the molybdenum (Mo, 3d), sulfur (S, 2p), carbon (C, 1s), oxygen (O, 1s), and nitrogen (N, 1s) elements. The exfoliated  $\text{MoS}_2$  nanosheets were biocompatible with the MG-63, MC3T3-E1, and C2C12 cells at 250  $\mu\text{g}/\text{mL}$  concentration. Further, microspheres were created using alginate, and they were characterized physiochemically and biologically. Stereomicroscopic images showed that the microspheres were spherical with an average diameter of  $1 \pm 0.2$  mm. The dispersion of  $\text{MoS}_2$  in the alginate matrix was uniform. The alginate- $\text{MoS}_2$  microspheres promoted apatite formation in the SBF (simulated body fluid) solution. Moreover, the alginate- $\text{MoS}_2$  was biocompatible with MG-63 cells and promoted cell proliferation. Higher alkaline phosphatase activity and mineralization were observed on the alginate- $\text{MoS}_2$  with the MG-63 cells. Hence, the developed alginate- $\text{MoS}_2$  microsphere could be a potential candidate for a bone graft substitute.



## INTRODUCTION

Bone injury or defects significantly affect the quality of human life. In orthopedic procedures, the most widely used grafting techniques to restore, repair, and regenerate damaged bone are autografts and allografts. However, these two grafting strategies suffer from several drawbacks like insufficient availability of donor tissue, need for secondary surgery, and disease transfer. As a result, much effort has gone into identifying an alternative to bone grafts. Bone tissue engineering is a multidisciplinary biomedical field that aims to develop artificial tissue as a clinical treatment method for repairing, preserving, and re-establishing damaged tissue.<sup>1</sup> In most cases, the implantation is performed with a scaffolding device, which provides physical support to the native tissue. Simultaneously, it encourages biological activities that aid in regenerating diseased or defective tissue. A biocompatible, biodegradable, and nontoxic material formed by combining materials, cells, and other small molecules is highly recommended in tissue engineering.<sup>2–4</sup> Tunable bioactive materials are often used to create artificial bone tissue (polymers, metals, alloys, and ceramics). Osteoconductive, osteoinductive, and mechanical strength are desirable properties to mimic bone tissues.<sup>5,6</sup> Nanoscale biomaterials effectively aid cellular growth, improve mechanical

strength, and impart osteoconductive and osteoinductive properties.<sup>7</sup>

Transition-metal dichalcogenides (TMDs) have gained much importance in biomedical fields such as tissue engineering, drug delivery, and biosensor application. Their intrinsic biocompatibility properties and their ability to interact favorably with cells and enhance mechanical strength are the primary reasons for their application. Bulk TMDs often do not exhibit attractive biological properties. However, the same materials at the nanoscale can favorably interact with cells for several biological applications. Molybdenum disulfide ( $\text{MoS}_2$ ) is a graphene-like TMD.<sup>8</sup> Due to its mechanical strength and biocompatibility,  $\text{MoS}_2$  has attracted tremendous interest in bone tissue engineering. Over the past few years, several techniques have developed nanostructured  $\text{MoS}_2$  using chemical vapor deposition, hydrothermal, solvothermal, and

Received: February 18, 2022

Accepted: July 6, 2022

Published: July 21, 2022



ACS Publications

liquid exfoliation methods.<sup>9–11</sup> Liquid-phase exfoliation of MoS<sub>2</sub> is achieved with intercalation, ultrasonication, and shear forces techniques.<sup>12–15</sup> Exfoliation of MoS<sub>2</sub> by using solvents, surfactants, polymers, and proteins is well recognized.<sup>16</sup> The liquid exfoliation method is simple, inexpensive, and scalable. Organic phase chemicals such as *N*-methylpyrrolidone (NMP) are often utilized to exfoliate MoS<sub>2</sub>, yet NMP-derived TMDs are often limited in biological applications due to the toxicity of NMP.<sup>17,18</sup> Protein-mediated (bovine serum albumin, silk fibroin, and keratin) liquid exfoliation proves advantageous in biological applications.<sup>19</sup> MoS<sub>2</sub> with hydroxyapatite<sup>20</sup> shows excellent cell proliferation, higher alkaline phosphatase activity (ALP), and induction of biominerization in bone marrow mesenchymal stem cells. Additionally, the up-regulation of osteocalcin (OCN), osteopontin (OPN), and Runt-related transcription factor (RUNX2) genes has been reported.<sup>13,20</sup>

Casein protein has gained much attention in tissue engineering applications because it is biocompatible, abundant, and inexpensive. Moreover, it has a bone-promoting effect.<sup>21,22</sup> As a result, several composite materials have been developed using casein and hydroxyapatite for bone tissue engineering with improved properties.<sup>23–25</sup>

Alginate (alginic acid) is an anionic polysaccharide comprising structural units of D-mannuronic (M) and L-guluronic (G) acids. Alginate is biocompatible, biodegradable, and nontoxic to cells, making it an essential candidate for bone tissue engineering applications. Furthermore, alginate can cross-link with divalent cations under mild conditions and can thus be fashioned into various scaffolding shapes. However, the utility of alginate in bone tissue regeneration is limited due to its lack of mechanical strength and cell-adhesive capabilities. As a result, an alginate-based scaffolding system is frequently coupled with additional materials for bone tissue engineering applications.<sup>26–29</sup> Microspheric scaffolds made of polymers for bone tissue engineering have advantages, including ease of preparation and nonrequirement of any highly sophisticated instruments. Additionally, these microspheres can hold/bind other ceramics, polymers, drugs, and growth factors that are used as sustainable drug delivery systems for bone tissue regeneration. The surface properties and porosity of microspheres significantly help cell adhesion and proliferation. Microspheres with alginate can be developed by an easy cross-linking method.<sup>30–32</sup>

This work aimed to prepare nanosheets of MoS<sub>2</sub> using casein. Furthermore, the alginate-based composite microspheres were engineered by incorporating casein-mediated liquid exfoliated MoS<sub>2</sub> nanosheets for bone tissue engineering. The physical and chemical characteristics of the microspheres were characterized. In addition, the cell viability, alkaline phosphatase activity, and mineralization potential of the microspheres were assessed on osteoblast-like cells.

## MATERIALS AND METHODS

Sodium alginate was purchased from Sigma-Aldrich (Steinheim Albuch, Germany). Molybdenum disulfide was purchased from Sigma-Aldrich (St. Louis, MO). Casein, sodium bicarbonate, and magnesium chloride hexahydrate were obtained from HiMedia Laboratories (Nashik, India). Calcium chloride, dipotassium hydrogen phosphate, hydrochloric acid, potassium chloride, sodium chloride, and sodium sulfate were purchased from Sigma-Aldrich (Bangalore, India). Ethanol was procured from Changshu Hongsheng Fine Chemicals Co., Ltd. (Yangyuan, China). MG-63, C2C12, and MC3T3-E1 cells

were procured from the National Centre for Cell Science (NCCS), Pune, India. Dulbecco's Modified Eagle's Medium (DMEM), phosphate-buffered saline (PBS), antibiotic–antimycotic solution, and L-glutamine were purchased from Gibco, Thermo Scientific (MA).

**Liquid Exfoliation of MoS<sub>2</sub> with Casein.** Exfoliation of layered MoS<sub>2</sub> was achieved utilizing a low energy-density sonic bath. In a typical batch, 50 mg of MoS<sub>2</sub> was mixed with 10 mg of casein in 10 mL of water (pH was adjusted to ~10 to dissolve the casein in water) and sonicated for 48 h. The resulting exfoliated solution was centrifuged for 45 min at 5000 rpm, and the casein–MoS<sub>2</sub> in the supernatant was collected (nano-MoS<sub>2</sub>-1). The remaining precipitate was redispersed in water and sonicated for 10 min. The resultant solution was centrifuged at 1500 rpm for 45 min, and the supernatant containing casein–MoS<sub>2</sub> nanosheets (nano-MoS<sub>2</sub>-2) was collected.

### Preparation of Alginate–Casein–MoS<sub>2</sub> Microspheres.

First, 3 g of sodium alginate was dissolved in 100 mL of distilled water with constant stirring using a magnetic stirrer for 1 h to obtain a homogeneous solution. Next, 10 mL of the alginate solution was taken in a 30 mL bottle, and 1 mL of casein–MoS<sub>2</sub> (10 mg/mL) was added and stirred for 4 h. Later, the solution was dropped into a 10% calcium chloride solution using a 5 mL syringe to form microspheres. These microspheres were continuously immersed in calcium chloride solution for the aging process. Microspheres were washed with water to remove unbound calcium chloride solution and air-dried, followed by freeze-drying. The developed microspheres were stored in a desiccator for further study.

### Chemical Characterization of the Exfoliated MoS<sub>2</sub>.

The formation of casein–MoS<sub>2</sub> exfoliation was confirmed using the Shimadzu UV spectrophotometer (Shimadzu, Kyoto, Japan) in the wavelength range of 200–800 nm using 10 mm quartz cuvettes at room temperature. The functional groups were determined by scanning the samples in an FT-IR spectrophotometer (Shimadzu, Kyoto, Japan) with a single reflection ATR (attenuated total reflectance) accessory in the 400–4000 cm<sup>−1</sup> wavelength range. Raman spectroscopy was performed for the casein–MoS<sub>2</sub> sample at room temperature with a Raman spectrometer (WITec alpha300 R, Germany). The X-ray diffraction (XRD) pattern of the casein–MoS<sub>2</sub> nanosheets was recorded using a Bruker D8 diffractometer with the Cu K $\alpha$  = 1.5406 Å radiation in the range of 20°–80° with a step size of 0.01. The morphologies and distribution of the exfoliated casein–MoS<sub>2</sub> nanosheets were investigated using high-resolution transmission electron microscopy (HR-TEM, JEM 2100, JEOL Ltd., MA). The size and thickness of the developed casein–MoS<sub>2</sub> nanosheets were measured using atomic force microscopy on the Park NX-10 instrument (Park Systems, NY). The X-ray photoelectron spectra (XPS) of the MoS<sub>2</sub> samples were collected on a Thermo Fisher ESCALAB QXi+ photoelectron spectrometer (Thermo Fisher Scientific, MA).

**Chemical Characterization of the Alginate–Casein–MoS<sub>2</sub> Microspheres.** Stereomicroscopic images of the developed microspheres were recorded on a ZEISS Stemi DV4 stereomicroscope (Carl Zeiss, Germany). The functional groups were determined by scanning the sample on the FT-IR spectrophotometer (Shimadzu, Kyoto, Japan) with a single reflection ATR accessory in a wavelength range of 400–4000 cm<sup>−1</sup>. The surface morphology of the developed microspheres was examined using a field emission scanning electron

microscope (FE-SEM, Carl Zeiss, Germany). The elements present in the microspheres were determined using energy-dispersive X-ray spectroscopy (EDS, Oxford instrumentation, ZEISS, UK). The XRD pattern of the developed microspheres was recorded using a Bruker D8 diffractometer using  $\text{Cu K}\alpha = 1.5406 \text{ \AA}$  radiation in the range of  $20^\circ\text{--}80^\circ$  with a step size of 0.01. The thermal stability of the developed microspheres was assessed by thermogravimetric analysis (TGA) and differential thermal analysis (DTA) using a Hitachi STA 7300 (Hitachi Instruments, Japan) instrument in the temperature range from 0 to  $750^\circ\text{C}$ .

**Evaluation of Mechanical Strength.** The compressive strength of the fabricated microspheres was measured using a universal strength testing machine (Tec-Sol INDIA, Chennai, India) equipped with a 2 kN load cell. The results were averaged over three specimens for each sample.<sup>33</sup>

**Water Uptake and Retention Ability.** To measure the ability of the microspheres to absorb water, they were weighed ( $W_{\text{dry}}$ ) and placed in a tube (Eppendorf) with distilled water for 24 h. The microspheres were then removed from the tubes, put on a Petri dish, and weighed ( $W_{\text{wet}}$ ). Finally, the water absorption capacity of the microspheres was estimated using the formula

$$\text{water uptake} = (W_{\text{wet}} - W_{\text{dry}})/W_{\text{dry}} \times 100$$

The water retention ability of the microspheres was measured by transferring wet microspheres to a centrifuge tube that had previously been loaded with filter paper at the bottom. The microspheres were immediately weighed after centrifugation at 500 rpm for about 3 min ( $W^1_{\text{wet}}$ ). The water retention ability of the microspheres was estimated using the formula<sup>34</sup>

$$\text{water retention} = (W^1_{\text{wet}} - W_{\text{dry}})/W_{\text{dry}} \times 100$$

**Protein Adsorption Study.** The microspheres were submerged in anhydrous ethanol in a 24-well plate for 1 h. After removal of the ethanol, the samples were treated for 30 min with 1× PBS. Later, 1× PBS was removed, and 500 mL of DMEM containing 10% FBS was added to the well plate. The samples were incubated for 6, 12, and 24 h to measure the protein adsorption effectiveness at defined time scales. The microspheres were dried by gentle blotting and washed three times with 1× PBS after each incubation to ensure the removal of loosely attached protein on the sample surface. The protein-adsorbed microspheres were stirred by incubation in a radioimmunoprecipitation buffer for 2 h at  $37^\circ\text{C}$ . The protein adsorption efficacy was measured using the Bradford standard calibration method with bovine serum albumin (BSA). Protein adsorbed on the microspheres was quantified using a UV spectrophotometer (Shimadzu, Kyoto, Japan) at a wavelength of 595 nm.<sup>35,36</sup>

**In Vitro Biodegradation Test.** The microspheres were soaked in a falcon tube containing 1× PBS with 100 U/L of lysozyme enzyme and oscillating at  $37^\circ\text{C}$ . For the next step, the microspheres were removed after 7, 14, 21, and 28 days, rinsed with deionized water, freeze-dried, and weighed again. The percentage of biodegradation ( $W_L$ ) was calculated using the following formula

$$W_L = (W_0 - W_1)W_0 \times 100$$

where  $W_0$  and  $W_1$  denote the weight of the microspheres before and after soaking in the solution, respectively. Three

replicates of each biocomposite microsphere were used for the study.<sup>37</sup>

**In Vitro Biomimetic Test.** The simulated body fluid (SBF) was prepared according to Kokubo's process to maintain a biological environment similar to that of the human body.<sup>38</sup> The microspheres were soaked in SBF and incubated at  $37^\circ\text{C}$  for 28 days. Each sample was gently cleaned with deionized water and dried in a desiccator. The production of biominerals on the surface of the microspheres was evaluated by FT-IR analysis and SEM-EDX analysis.

**Cell Viability Assay.** The biocompatibility of the produced microspheres was tested with MG-63 cells using the MTT (3-(4,5-dimethylthiazol-2-yl)-2,5-diphenyltetrazolium bromide) assay. For the assay,  $5 \times 10^3$  cells were seeded per well in a 96-well plate. After cell adherence, 25, 50, 100, 250, and 500  $\mu\text{g}/\text{mL}$  of the microspheres were added and incubated for 48 h at  $37^\circ\text{C}$  in a 5%  $\text{CO}_2$  humidified atmosphere. The cells were then treated with 100  $\mu\text{L}$  of 1 mg/mL MTT solution and incubated for 3 h. Formazan crystals were dissolved using 100  $\mu\text{L}$  of DMSO, and the absorbance was measured at 570 nm.<sup>39</sup> The same steps were followed to check the biocompatibility of the liquid exfoliated casein–MoS<sub>2</sub> with the MG-63, MC3T3-E1, and C2C12 cells.

**Acridine Orange and Ethidium Bromide (AO/EB) Double-Staining Assay.** The AO/EB staining assay was performed according to a previous report.<sup>40</sup> Briefly,  $1 \times 10^4$  cells/well were seeded into 24-well plates and incubated for 24 h at  $37^\circ\text{C}$  in 5%  $\text{CO}_2$  in a humidified atmosphere. Wells containing only the culture medium served as the control group. Microspheres (500  $\mu\text{g}/\text{mL}$ ) were introduced, and the plate was incubated for 24 h at  $37^\circ\text{C}$  and 5%  $\text{CO}_2$  in a humidified atmosphere. Further, the used media were discarded, and the cells were stained for 15 min at  $37^\circ\text{C}$  in the dark with an acridine orange–ethidium bromide composite dye mixture (1:1). The excess stain was removed, and the stained cells were overlaid with PBS. The cells were photographed in red and green channels using a ZOE Fluorescence Cell Imager (ZOE, BioRad, USA).

**Hoechst 33342 Staining Assay.** For this assay,  $1 \times 10^4$  cells/well were seeded into 24-well plates and incubated for 24 h at  $37^\circ\text{C}$  in a 5%  $\text{CO}_2$  humidified atmosphere. All three microspheres with 500  $\mu\text{g}/\text{mL}$  concentrations were introduced to the cells and incubated for 24 h. Later, the excess media were withdrawn, and the cells were stained with bisBenzimide Hoechst 33342 dye solution (5  $\mu\text{g}/\text{mL}$ ) to stain the cell nuclei. The plate was then incubated for 15 min at  $37^\circ\text{C}$ . The excess dye was removed, and the cells were rinsed thrice with PBS. PBS was placed on the cells, and images were recorded using the ZOE Fluorescence Cell Imager under the blue channel (ZOE, BioRad, USA).

**Alkaline Phosphatase Assay.** Osteoblast differentiation of the MG-63 cells with the developed microspheres was examined using the alkaline phosphatase (ALP) assay.<sup>41</sup> Briefly,  $10 \times 10^3$  cells per well were cultured in a 24-well plate. After cell attachment, 100, 250, and 500  $\mu\text{g}/\text{mL}$  concentrations of microsphere samples were introduced and maintained for 7 and 14 days in the humidified incubator at  $37^\circ\text{C}$  and 5%  $\text{CO}_2$ . Additionally, media containing osteogenic supplements were provided once every 2 days. Further, the cells were washed with PBS, and supplemented with carbonate buffer (100  $\mu\text{L}$ , 25 mM, pH 10.3) comprising Triton X-100 (0.2%). Next, carbonate buffer (50  $\mu\text{L}$ , 250 mM, pH 10.3) with 2.5 mM MgCl<sub>2</sub> and 15 mM p-nitrophenyl phosphate were

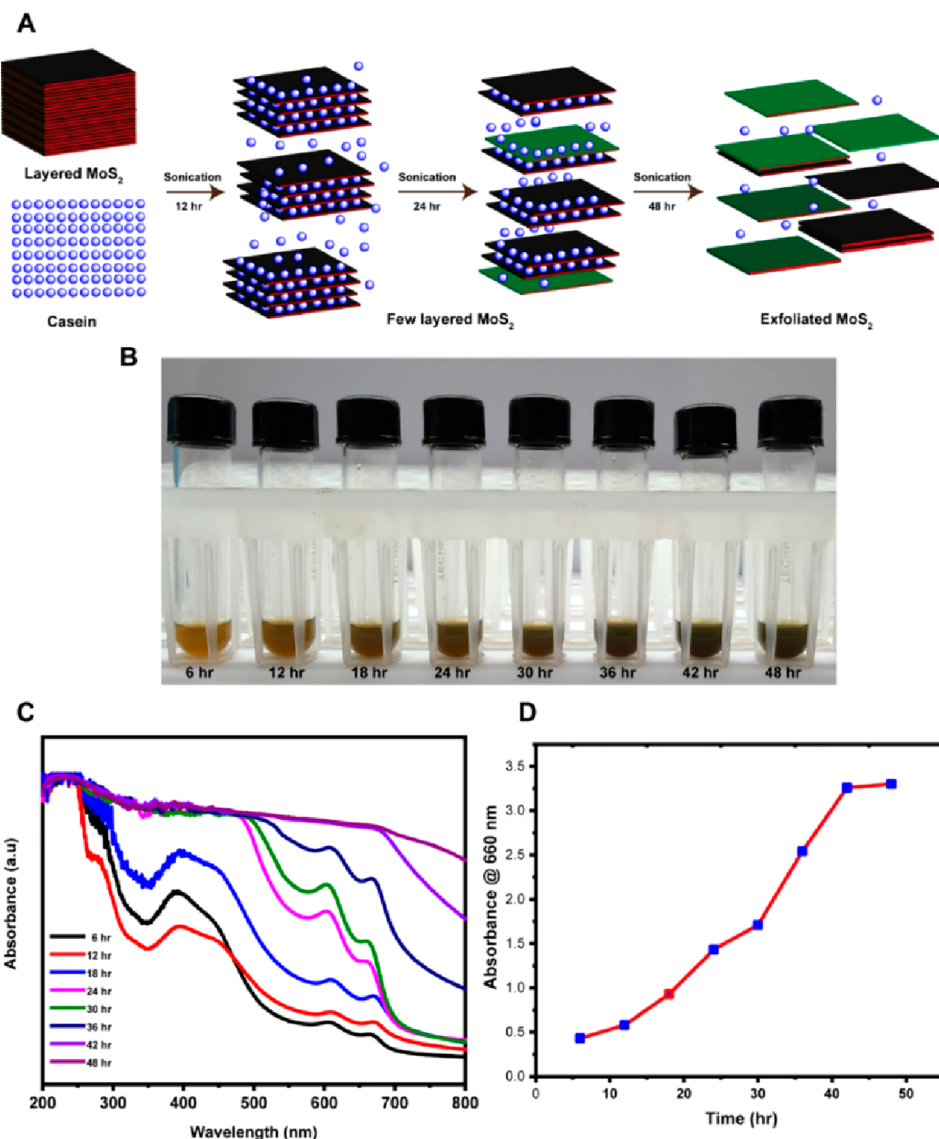


**Figure 1.** (A) Schematic depiction of the exfoliation of MoS<sub>2</sub> with casein. (B) Visual observations of the exfoliated nano-MoS<sub>2</sub> solution at different time intervals. (C) UV-vis spectra of the exfoliated nano-MoS<sub>2</sub> at different time intervals. (D) Absorbance of the exfoliated nano-MoS<sub>2</sub> at 660 nm at different time intervals.

added to each well. Later, the plate was incubated at 37 °C for 30 min, and finally, the absorbance values were measured by a fluorescence microplate reader at 405 nm (FLUOstar Omega, BMG LABTECH, Germany).

**Alizarin Red S Assay.** The formation of minerals on the MG-63 cell lines with the developed microspheres was detected by the Alizarin Red S assay. In a 6-well plate, 2 × 10<sup>4</sup> cells were grown in each well. After cell adhesion, 500 µg/mL concentrations of microsphere samples were administered and maintained in a humidified incubator at 37 °C and 5% CO<sub>2</sub> for 7 and 14 days. The media containing osteogenic supplements were changed every 2 days, and the media were removed after the completion of the incubation time. First, cells were washed twice with PBS and fixed in 4% formaldehyde for 1 h at room temperature. Next, the cells were stained with 40 mM Alizarin Red S (pH 4.1) for 10 min. Further, the cells were washed twice with PBS before incubating for 15 min in 10 mM sodium phosphate buffer (pH 7.0) containing 10% cetylpyridinium chloride. Finally, the

absorbance of the solution was measured at 562 nm (FLUOstar Omega, BMG LABTECH, Germany).

**Statistical Analysis.** The quantitative data of all experiments were analyzed with the OriginPro 2017 software. The GraphPad Prism version 8 software was used to plot the graphs and perform the statistical analyses. All of the data were expressed as the mean ± standard deviation (SD).

## RESULTS AND DISCUSSION

**Exfoliation of MoS<sub>2</sub> with Casein.** The scheme for MoS<sub>2</sub> exfoliation with casein is shown in Figure 1A. The visual observations of the exfoliated nano-MoS<sub>2</sub> nanosheet suspensions at various time intervals are compiled as photographs in Figure 1B. The solution turned progressively darker green with increased sonication time, which indicated the formation of the MoS<sub>2</sub> nanosheets. The production of casein-mediated, exfoliated nano-MoS<sub>2</sub> was confirmed using UV-visible spectroscopy (Figure 1C). The nanosheets of MoS<sub>2</sub> exhibited absorption peaks at 610 and 668 nm (Figure 1C). Thus, UV-

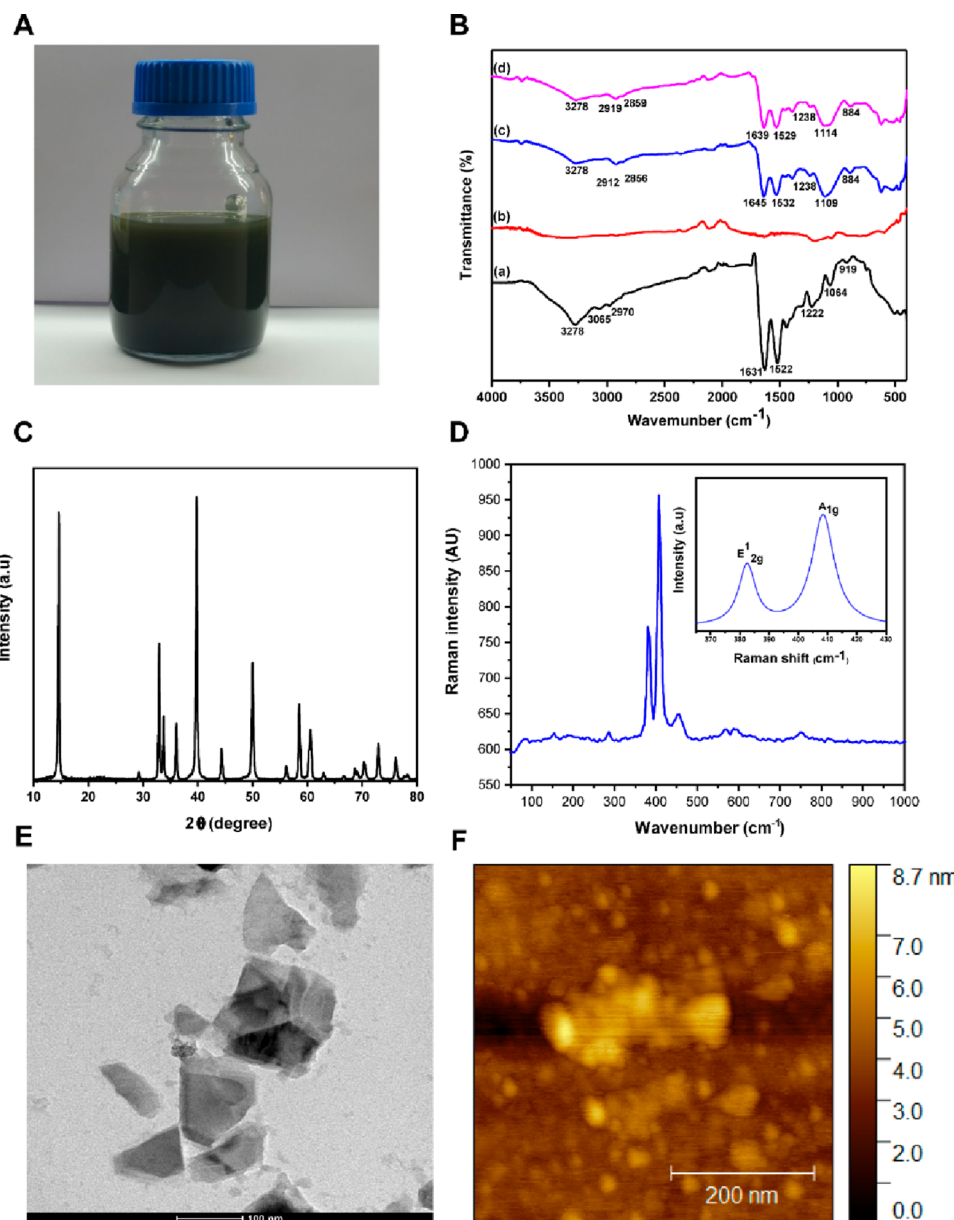


**Figure 2.** (A) Bulk production of nano-MoS<sub>2</sub> with casein (100 mL batch). (B) FT-IR spectrum of (a) casein, (b) commercial MoS<sub>2</sub>, (c) casein nano-MoS<sub>2</sub>-1, and (d) casein nano-MoS<sub>2</sub>-2. (C) XRD spectrum of exfoliated nano-MoS<sub>2</sub>-2. (D) Raman spectra of exfoliated nano-MoS<sub>2</sub>-2. (E) HR-TEM images of exfoliated nano-MoS<sub>2</sub>-2. (F) AFM images of exfoliated nano-MoS<sub>2</sub>-2.

visible absorption spectrum data revealed that casein helped to form MoS<sub>2</sub> nanosheets by sonication.<sup>12</sup> The production of nanostructured MoS<sub>2</sub> at various time intervals at 660 nm absorbance is shown in Figure 1D. The absorbance in the Y-axis increased with time. The maximum nanostructured MoS<sub>2</sub> exfoliated with casein was observed at 48 h of sonication. Therefore, mild sonication was necessary to exfoliate with a good yield in a 100 mL batch (Figure 2A). The dispersion stability of casein–MoS<sub>2</sub>-2 in water on different days (a) sixth day, (b) 12th day, (c) 18th day, and (d) 24th day is shown in Figure S2. Wang et al. developed chitosan-embedded ultrathin MoS<sub>2</sub> nanosheets. They identified the characteristic peaks at 615 and 675 nm using UV spectroscopy, which confirmed the existence of nano-MoS<sub>2</sub>.<sup>42</sup> In another study, Agarwal et al. developed keratin-assisted nano-MoS<sub>2</sub>, wherein the formation of the nanosheets was confirmed by UV-vis analysis.<sup>19</sup> Dolai et al. confirmed the presence of a characteristic peak in the

range of 600–800 nm in the UV analysis for the existence of nano-MoS<sub>2</sub>.<sup>43</sup>

**Chemical Characterization of MoS<sub>2</sub>.** The FT-IR spectrum of casein is shown in Figure 2B (a). A characteristic peak at 3278 cm<sup>-1</sup> confirmed the presence of the –OH group. The vibrational bond peaks at 3065 and 2970 cm<sup>-1</sup> belonged to the symmetric and asymmetric stretching of the –CH<sub>2</sub> group, respectively. The peaks in the 1300–1000 cm<sup>-1</sup> range belonged to the carbonyl group. Further, peaks at 1631 and 1522 cm<sup>-1</sup> belonged to the amide group.<sup>44</sup> However, no characteristic peak was observed for the commercial bulk MoS<sub>2</sub>. The FT-IR spectra of the exfoliated nano-MoS<sub>2</sub> are shown in Figures 2B (b), (c), and (d). The vibrational bands at 3278, 2912, 2856, 1645, 1532, 1238, 1109, and 884 cm<sup>-1</sup> belonged to the exfoliated nano-MoS<sub>2</sub>-1 with casein. Similar peaks were observed for the exfoliated nano-MoS<sub>2</sub>-2.

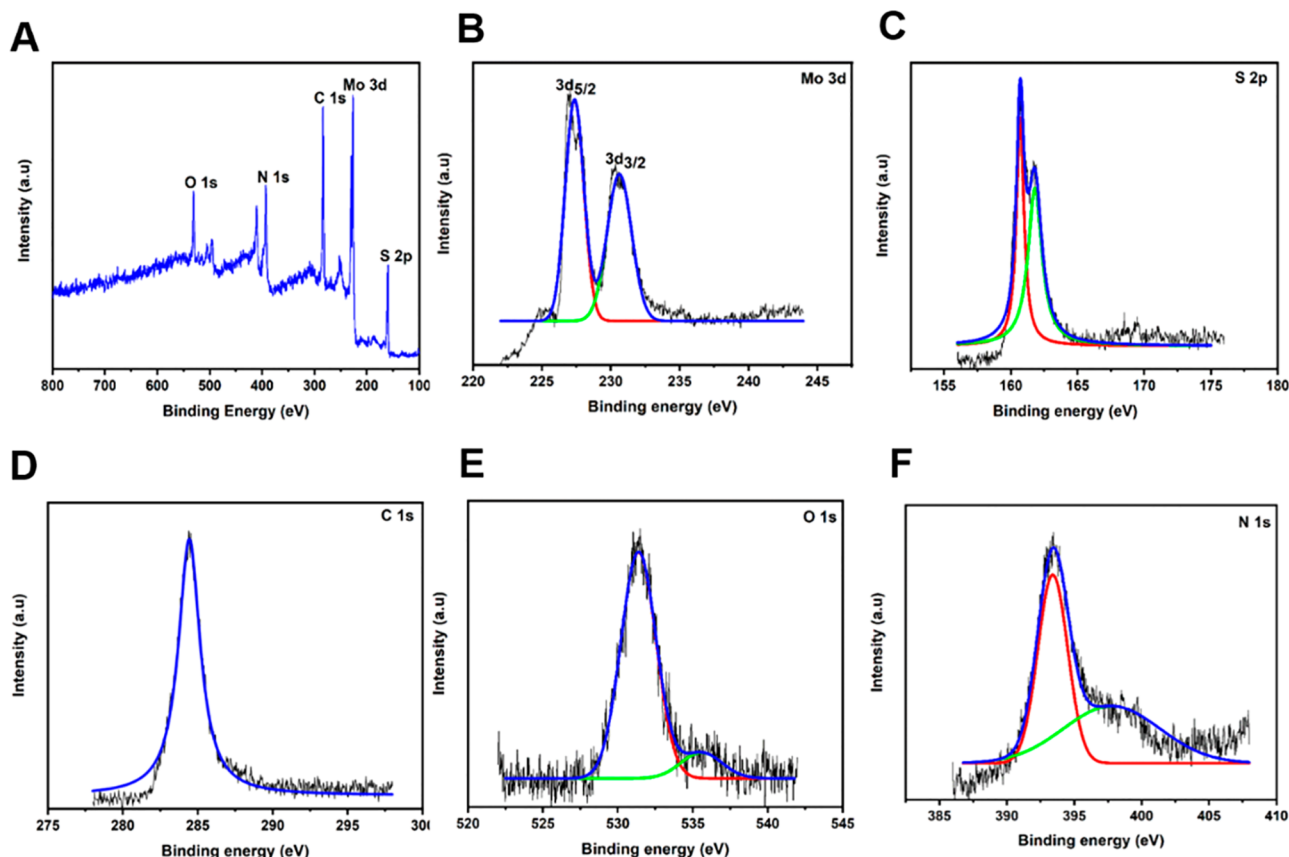


**Figure 3.** XPS analysis of the developed nano-MoS<sub>2</sub>-2 and the individual elemental image: (A) nano-MoS<sub>2</sub>-2; (B) Mo, 3d; (C) S, 2p; (D) C, 1s; (E) O, 1s; and (F) N, 1s.

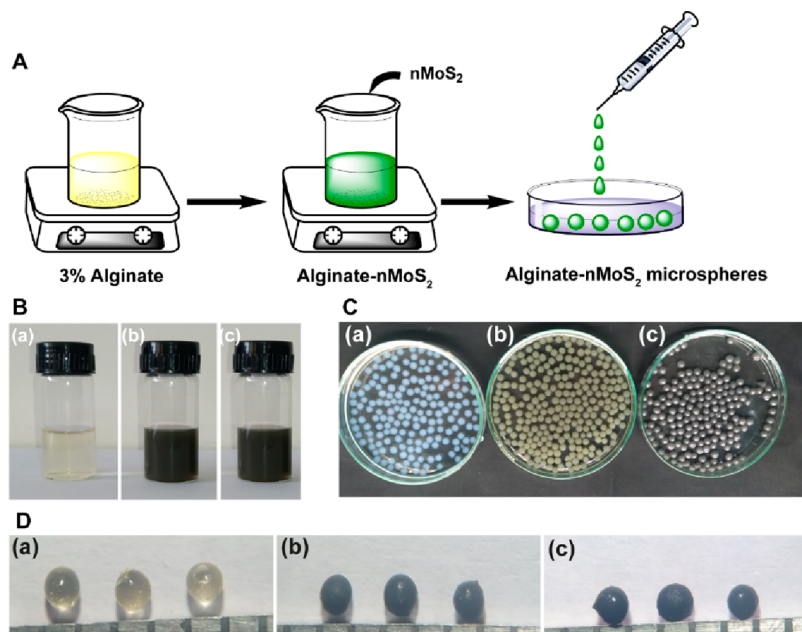


**Figure 4.** (A) Schematic representation of the development of microspheres. (B) Photographs of solution of (a) alginate, (b) alginate-MoS<sub>2</sub>-1, and (c) alginate-MoS<sub>2</sub>-2. (C) Photographs of the microspheres of (a) alginate, (b) alginate-MoS<sub>2</sub>-1, and (c) alginate-MoS<sub>2</sub>-2. (D) stereomicrographs of (a) alginate, (b) alginate-MoS<sub>2</sub>-1, and (c) alginate-MoS<sub>2</sub>-2.

The XRD pattern of the developed nano-MoS<sub>2</sub>-2 is illustrated in Figure 2C. The (002), (100), (103), (105), and (110) at  $2\theta$  values of 14.6, 32.9, 39.7, 49.9, and 58.4, respectively, belonged to the pure hexagonal nano-MoS<sub>2</sub>.<sup>45,46</sup>

Raman spectroscopy is an important technique to identify the molecules by matching the vibrational modes of the molecules. The Raman spectrum of the nano-MoS<sub>2</sub>-2 is demonstrated in (Figure 2D). The significant peaks at 382 and 408 cm<sup>-1</sup> are

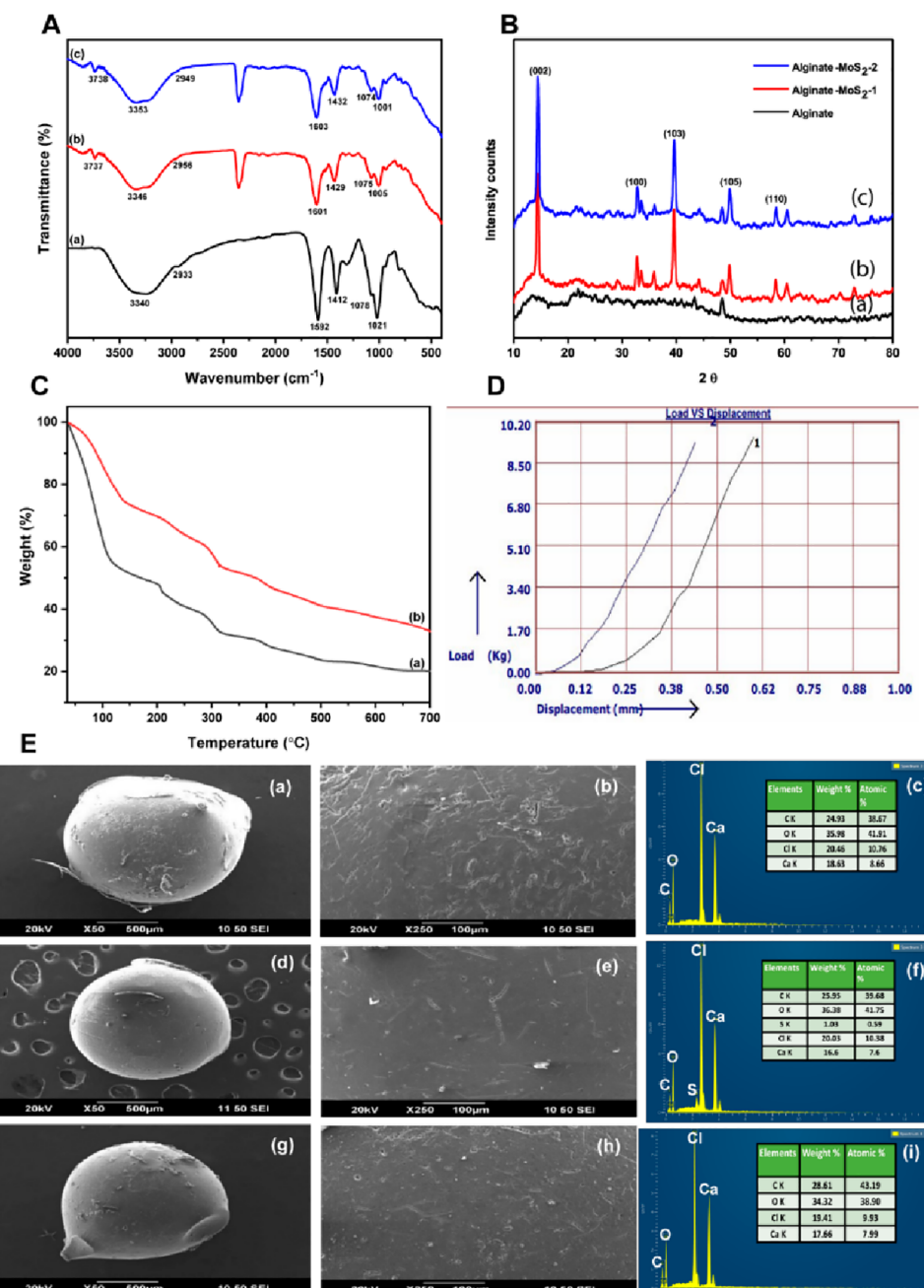


**Figure 5.** (A) FT-IR spectrum of (a) alginate, (b) alginate–MoS<sub>2</sub>-1, and (c) alginate–MoS<sub>2</sub>-2. (B) XRD patterns of (a) alginate, (b) alginate–MoS<sub>2</sub>-1, and (c) alginate–MoS<sub>2</sub>-2. (C) TGA graph of (a) alginate and (b) alginate–MoS<sub>2</sub>-1. (D) Mechanical strength of the developed microspheres (alginate–MoS<sub>2</sub>-2). (E) High- and low-magnification FE-SEM images and corresponding EDS spectra of alginate (a, b, and c), alginate–MoS<sub>2</sub>-1 (d, e, and f), and alginate–MoS<sub>2</sub>-2 (g, h, and i).

accompanied by the MoS<sub>2</sub> vibrational modes of in-plane E<sub>2g</sub><sup>1</sup> and out-of-plane A<sub>1g</sub>, respectively.<sup>12,47,48</sup>

The HR-TEM images of the exfoliated nanosheets are shown in Figure 2E. Flakes of dispersed nano-MoS<sub>2</sub> with diameters in the nanometer range are visible in the micrographs. Sim et al. reported the development of exfoliated nano-MoS<sub>2</sub> using freeze-dried silk fibroin powder by the sonication method. TEM results of exfoliated MoS<sub>2</sub> exhibited a diameter of 200 nm.<sup>49</sup> In another study, alginate-assisted exfoliated MoS<sub>2</sub> nanosheets were developed, and HR-TEM analysis indicated that the nanosheets retained their lattice structure after exfoliation.<sup>50</sup> Huang et al. developed exfoliated molybdenum diselenide, and HR-TEM analysis revealed the

produced nanosheets with an average diameter of around 100 nm.<sup>51</sup> The atomic force microscopic image of exfoliated nano-MoS<sub>2</sub> is shown in Figure 2F.<sup>42,52</sup> The results of the (A) DLS spectrum, (B) XRD pattern, (C) TEM images, and (D) atomic force microscopy image of the nano-MoS<sub>2</sub>-1 nanosheet are shown in Figure S1. The results confirmed the formation of the MoS<sub>2</sub> nanosheets.

The chemical composition of the produced exfoliated nano-MoS<sub>2</sub> was determined using XPS analysis (Figure 3). All components found in nano-MoS<sub>2</sub>-2 are shown in Figure 3A. The elements molybdenum (Mo, 3d), sulfur (S, 2p), carbon (C, 1s), oxygen (O, 1s), and nitrogen (N, 1s) are, respectively, shown in Figure 3B, C, D, E, and F. In the XPS spectra of the

nano-MoS<sub>2</sub>-2, the above elements (Mo, 3d; S, 2p; C, 1s; O, 1s; and N, 1s) were detected at binding energy (eV) values of 227, 160, 284, 531, and 393, respectively. This figure indicates that casein has mobilized into MoS<sub>2</sub>, and it stabilizes the nano-MoS<sub>2</sub>.<sup>53–56</sup> Hu et al. developed nano-MoS<sub>2</sub> using a simple homogeneous precipitation process. XPS examination revealed the existence of chemical components in the nano-MoS<sub>2</sub>.<sup>57</sup>

**Fabrication of Alginate–Nano-MoS<sub>2</sub> Microspheres.** The schematic representation of the microsphere production with 3% alginate and exfoliated nano-MoS<sub>2</sub> is shown in Figure 4A. The color change in the solution after MoS<sub>2</sub> addition is shown in Figure 4B. The nanosheets remained well dispersed without any sedimentation after addition of nano-MoS<sub>2</sub> to the alginate solution. Thus, the exfoliated nano-MoS<sub>2</sub> was highly stable in the alginate solution. The photographs of the microspheres of (a) clear alginate, (b) alginate–MoS<sub>2</sub>-1, and (c) alginate–MoS<sub>2</sub>-2 of different particle sizes are shown in Figure 4C. The size and surface appearance of the generated microspheres were studied using a stereomicroscope. The dried microspheres with 3% alginate appeared light yellow (Figure 4D (a)), whereas alginate microspheres containing the nanosheets of MoS<sub>2</sub>-1 and MoS<sub>2</sub>-2 were black (Figure 4D (b and c)). Further, all microspheres appeared spherical with an average diameter of  $1 \pm 0.2$  mm, as deduced from the stereomicroscopic images.<sup>58–60</sup>

**Chemical Characterization of the Microspheres.** **Fourier-Transform Infrared Spectroscopy Analysis.** The FT-IR spectra of alginate, alginate–MoS<sub>2</sub>-1, and alginate–MoS<sub>2</sub>-2 microspheres are compiled in Figure 5A (a, b, and c). The absorption peak at 3340 cm<sup>-1</sup> belongs to the –OH group, and the peak at 2933 cm<sup>-1</sup> represents the C–H stretch group (Figure 5A (a)). The vibrational peak at 1592 cm<sup>-1</sup> corresponds to the carbonyl group (C=O). In addition, the characteristic peak at 1412 cm<sup>-1</sup> belongs to the symmetric carboxylic group (–COOH). In addition, the absorption peaks at 1078 and 1021 cm<sup>-1</sup> correspond to the asymmetric carboxylic group. The absorption peaks at 3346, 2956, 1601, 1429, 1075, and 1005 cm<sup>-1</sup> in Figure 5A (b) belong to 3% alginate–MoS<sub>2</sub>-1. Further, the peaks at 3353, 2949, 1603, 1432, 1074, and 1001 cm<sup>-1</sup> in Figure 5A (c) correspond to 3% alginate–MoS<sub>2</sub>-2. All peaks related to 3% alginate displayed a slight shift in Figures 5A (b and c). The results indicated the presence of interactions between alginate and exfoliated nano-MoS<sub>2</sub>.<sup>44,61</sup>

**XRD Analysis.** The XRD patterns of alginate (a), alginate–MoS<sub>2</sub>-1 (b), and (c) alginate–MoS<sub>2</sub>-2 are shown in Figure 5B. In the diffraction pattern of 3% alginate microspheres, a broad peak was detected at  $2\theta$  values of 13 and 23, confirming the presence of alginate (Figure 5B (a)). Alginate–MoS<sub>2</sub>-1 and alginate–MoS<sub>2</sub>-2 microspheres showed peaks at  $2\theta$  values of 14, 33, 39, 49, and 59, obtained from nano-MoS<sub>2</sub>. Additionally, a broad peak was found at a  $2\theta$  value of 23 (Figures 5B (b and c)), which arose from the alginate moieties.<sup>62,63</sup> Wu et al. fabricated nanofibers containing polycaprolactone and MoS<sub>2</sub> for bone regeneration application. Further, the incorporation of MoS<sub>2</sub> in the polycaprolactone was confirmed by XRD analysis.<sup>64</sup> Gum tragacanth, poly(vinyl alcohol), and MoS<sub>2</sub> were developed for biomedical applications. A sharp peak was observed for the crystalline plane (002) in the XRD analysis, which revealed the existence of MoS<sub>2</sub>.<sup>65</sup>

**Thermal Gravimetric Analysis (TGA) of the Developed Microspheres.** The thermal stability of the developed microspheres was examined with TGA (Figure 5C). Deflection

peaks were observed at 109, 202, 282, 306, and 395 °C for the 3% alginate microspheres (Figure 5C (a)). The first deflection peak, almost at 109 °C, is associated with the water's loss of moisture and dehydration. Subsequent deflections at 202, 282, 306, and 395 °C arose from the degradation of the sodium alginate. Deflection peaks of sodium alginate at 112, 216, 293, 309, and 396 °C indicated that the inclusion of the MoS<sub>2</sub> nanosheets in the alginate beads enhanced the thermal stability of the polymer.

Furthermore, compared to microspheres of neat alginate and nanosheets of MoS<sub>2</sub>, the weight reduction in the composite microspheres of 3% alginate and nanosheets of MoS<sub>2</sub> was lower.<sup>66,67</sup> Coradin and his colleagues fabricated a biocomposite combining alginate and silica. TGA revealed that the thermal breakdown of the alginate occurs at temperatures below 500 °C.<sup>68</sup> They developed a nanocomposite film incorporating sodium alginate and graphene oxide. TGA revealed increased film thermal stability upon increasing the percentage of graphene oxide.<sup>69</sup> These studies corroborated the TGA results of the microspheres in the present study, indicating improved thermal stability upon adding MoS<sub>2</sub> nanosheets to sodium alginate.

**Mechanical Strength of the Developed Microspheres.** The scaffolding system applied in bone tissue engineering should have mechanical strength comparable to the host bone tissue, allowing the body to bear weight until new bone tissue is regenerated. The compressive strength of human cortical bone ranges from 90 to 209 MPa, while cancellous bone has a compressive strength of 1.5 to 45 MPa. The compressive strength of the developed microspheres was closer to that of the native bone. Alginate–MoS<sub>2</sub>-1 and alginate–MoS<sub>2</sub>-2 microspheres displayed compressive strengths of 69.75 MPa, and 71.38 MPa, respectively.<sup>70,71</sup> Thus, the developed microspheres were mechanically compatible for bone tissue engineering applications.

**FE-SEM and EDAX Analysis of the Developed Microspheres.** The surface morphology of the alginate, alginate–MoS<sub>2</sub>-1, and alginate–MoS<sub>2</sub>-2 microspheres was studied using high and low magnification FE-SEM (Figure 5E (a and b), 5E (d and e), and 5E (g and h), respectively). No change was observed in the morphology of the microspheres because they contained a higher percentage of alginate. The results of the EDAX analysis of the elements present in the alginate, alginate–MoS<sub>2</sub>-1, and alginate–MoS<sub>2</sub>-2 microspheres are shown in Figure 5E (c, f, and i).<sup>72,73</sup>

**Water Uptake and Retention Ability of the Developed Microspheres.** Water uptake and retention of the composite scaffolds are critical parameters for materials that are implanted in the body for fluid absorption and the transport of cell nutrients and metabolites.<sup>34,70</sup> The water uptake and retention ability of the developed microspheres is shown in Figure 6A. The microspheres exhibited a higher potential to absorb and retain water than their weight. Alginate microspheres incorporating nanosheets of MoS<sub>2</sub>-1 and MoS<sub>2</sub>-2 possessed considerably higher water absorption (~1.22 higher) and retention (~1.28 higher) abilities than the neat alginate microspheres. The addition of MoS<sub>2</sub> nanosheets improved the water uptake and retention capabilities of the produced microspheres. Thus, the composite microspheres would help in transporting nutrients and metabolites.<sup>34,70</sup> Purohit et al. performed a study on the swelling ratio of a scaffold containing gelatin–alginate–graphene oxide. The swelling ratio of the nanocomposites (~700%) in 14 h indicated that the developed

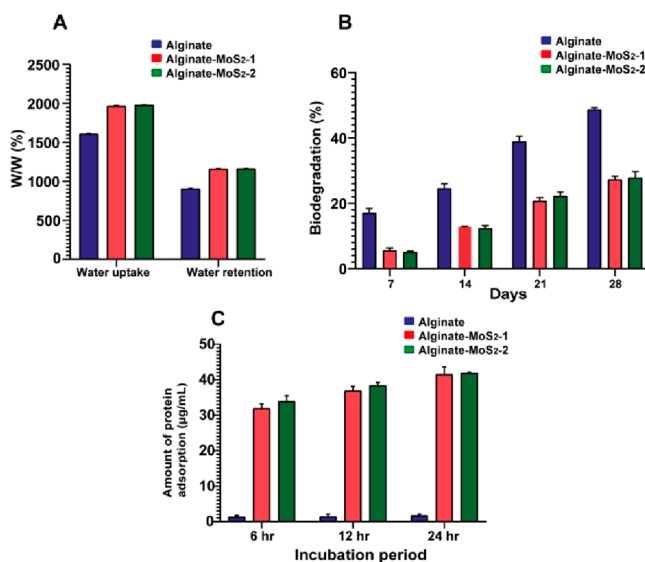


**Figure 6.** (A) Water uptake and retention of the developed microspheres containing 3% alginate, alginate–MoS<sub>2</sub>-1, and alginate–MoS<sub>2</sub>-2. (B) Biodegradation results of 3% alginate, 3% alginate–MoS<sub>2</sub>-1, and alginate–MoS<sub>2</sub>-2 biocomposite microspheres. (C) Protein adsorption studies of the alginate–MoS<sub>2</sub>-1 and alginate–MoS<sub>2</sub>-2 composite microspheres.

scaffold was hydrophilic and can help in tissue engineering applications.<sup>37</sup>

**In Vitro Biodegradation of the Developed Microspheres.** The slow degradation of the scaffold is an essential parameter for osseointegration, cell growth, and tissue regeneration.<sup>74</sup> The *in vitro* biodegradation of the developed microspheres was measured in terms of weight loss (%) in PBS and lysozyme after incubation at different times at 37 °C (Figure 6B). Alginate microspheres showed 17% degradation after 7 days of incubation, whereas the alginate–MoS<sub>2</sub>-1 and –MoS<sub>2</sub>-2

microspheres showed 5% degradation. Moreover, after 28 days of incubation, the degradation rate of the alginate microspheres increased to 48%, whereas the degradation rate of the microspheres containing alginate–MoS<sub>2</sub>-1 and –MoS<sub>2</sub>-2 increased to 27%. This finding suggested that the microspheres containing alginate–MoS<sub>2</sub>-1 and –MoS<sub>2</sub>-2 possessed a relatively lower controllable biodegradation rate than microspheres containing only 3% alginate. Biodegradation results also indicated the strong chemical interaction between alginate and MoS<sub>2</sub> nanosheets.<sup>36,37,75,76</sup>

**Protein Adsorption Study on the Developed Microspheres.** Protein adsorption on the scaffold can facilitate cell adhesion and proliferation and stimulate bone tissue regeneration.<sup>77</sup> The amounts of bovine serum albumin (BSA) proteins adsorbed on the developed microspheres are shown in Figure 6C. Alginate microspheres absorbed 1.3 μg/mL of protein after 6 h of incubation. Furthermore, the protein adsorption on these microspheres after 24 h of incubation was 1.65 μg/mL; a marginal increase was observed in the protein adsorption with increased incubation time. Alginate–MoS<sub>2</sub>-1 and alginate–MoS<sub>2</sub>-2 microspheres adsorbed more than 32 μg/mL of protein, which increased with time. The developed microspheres absorbed nearly 42 μg/mL after 24 h of incubation. Incorporating exfoliated nano-MoS<sub>2</sub> in alginate improved protein adsorption, facilitating cell adhesion and proliferation.

**In Vitro Biomimetic Study on the Developed Microspheres.** *In vitro* biomimetic capacity of the scaffold ensures its bone-bonding capability. Stereomicroscopic images of the microspheres after *in vitro* biomimetic study are shown in Figure 7. The alginate microspheres exhibited less mineral deposition (Figure 7A (a)). The formation of the apatite layer was visible on the surface of the developed alginate–MoS<sub>2</sub>-1 and alginate–MoS<sub>2</sub>-2 microsphere scaffolds in simulated body fluid (SBF) (Figures 7A (b and c)). In an earlier study, exfoliated nano-MoS<sub>2</sub> was incorporated in

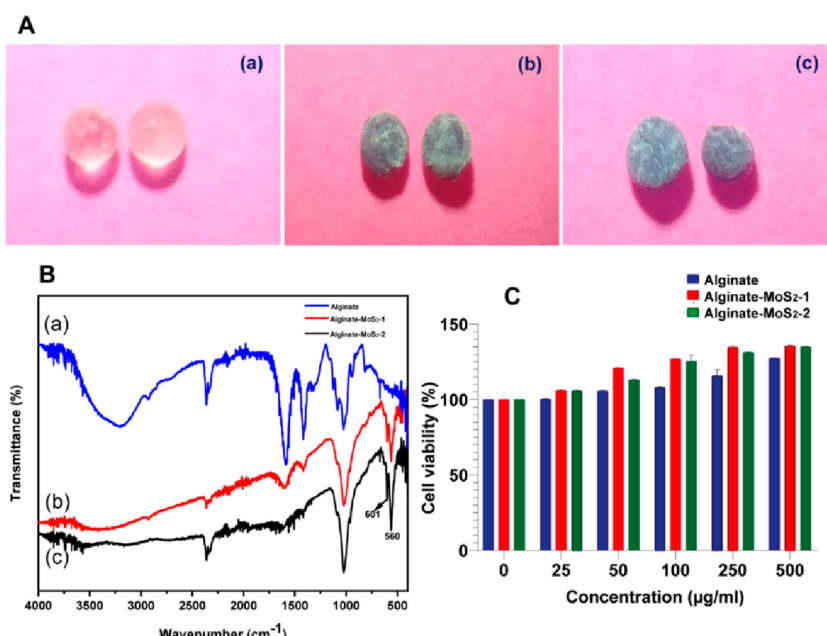


**Figure 7.** (A) Stereo-microscopic images of the microspheres after immersion in SBF: (a) alginate, (b) alginate–MoS<sub>2</sub>-1, and (c) alginate–MoS<sub>2</sub>-2. (B) FT-IR spectrum of microspheres after immersion in SBF: graph (a) alginate, (b) alginate–MoS<sub>2</sub>-1, (c) alginate–MoS<sub>2</sub>-2; and (C) MTT assay results with MG-63 osteoblast-like cells at different concentrations of the microspheres, measured using three independent values.

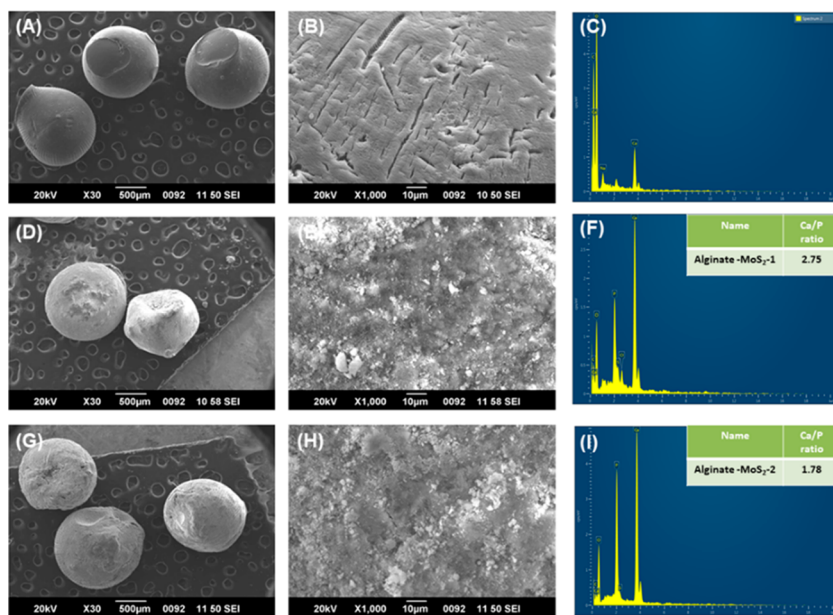


**Figure 8.** FE-SEM-EDX images (A, B) for 3% alginate at 500 and 10  $\mu\text{m}$  magnifications, respectively; images (D, E) for alginate-nano-MoS<sub>2</sub>-1 at 500 and 10  $\mu\text{m}$  magnifications, respectively; images (G, H) for alginate-nano-MoS<sub>2</sub>-2 at 500 and 10  $\mu\text{m}$  magnifications, respectively; images (C, F) and (I) EDX images of 3% alginate, alginate-nano-MoS<sub>2</sub>-1, and alginate-nano-MoS<sub>2</sub>-2, respectively.

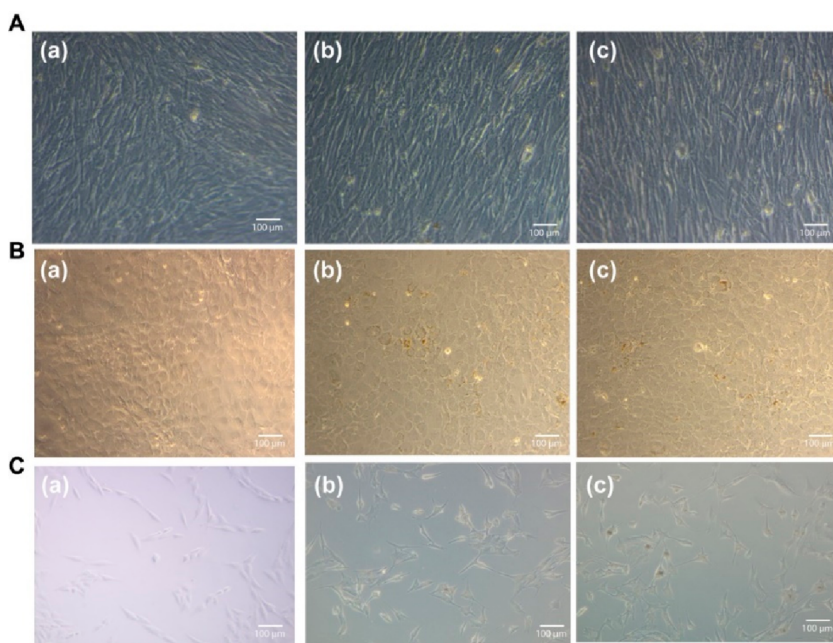


**Figure 9.** Optical micrographs of (A) C2C12 cells, (B) MC3T3-E1 cells, and (C) MG-63 cells after treatment with (a) control, (b) 50  $\mu\text{g}/\text{mL}$  of exfoliated nano-MoS<sub>2</sub>-2, and (c) 250  $\mu\text{g}/\text{mL}$  of exfoliated nano-MoS<sub>2</sub>-2.

polycaprolactone and zein for bone regeneration. The *in vitro* biominerization of SBF showed that MoS<sub>2</sub> composites promote mineralization.<sup>13</sup>

FT-IR spectra of the alginate, alginate-MoS<sub>2</sub>-1, and alginate-MoS<sub>2</sub>-2 microspheres after immersion in SBF are shown in Figure 7B. The alginate microspheres formed fewer mineral nodules. The peak at nearly 560  $\text{cm}^{-1}$  belongs to the phosphate group (Figure 7B (a)). These results suggested that microspheres containing alginate with nano-MoS<sub>2</sub>-1 and nano-MoS<sub>2</sub>-2 can induce mineralization.<sup>78</sup>

SEM/EDX analyses were performed to identify biominerization on the developed microspheres. The SEM images of

the 3% alginate, alginate-MoS<sub>2</sub>-1, and alginate-MoS<sub>2</sub>-2 microspheres are represented in Figure 8 A,B, 8E, and 8G,H, respectively. The solution of only 3% alginate microspheres did not form an apatite layer on the surface. However, a solid and thick apatite layer was observed on the surface of the alginate-MoS<sub>2</sub>-1 and alginate-MoS<sub>2</sub>-2 microspheres. From the SEM results, alginate-MoS<sub>2</sub>-1 and alginate-MoS<sub>2</sub>-2 microspheres appeared to have a stronger potential to promote apatite production. Further, to detect the mineral deposition content on the developed microspheres, EDX analysis was performed. Calcium (Ca) and phosphate (P) elements were observed on the alginate-MoS<sub>2</sub>-1 and alginate-

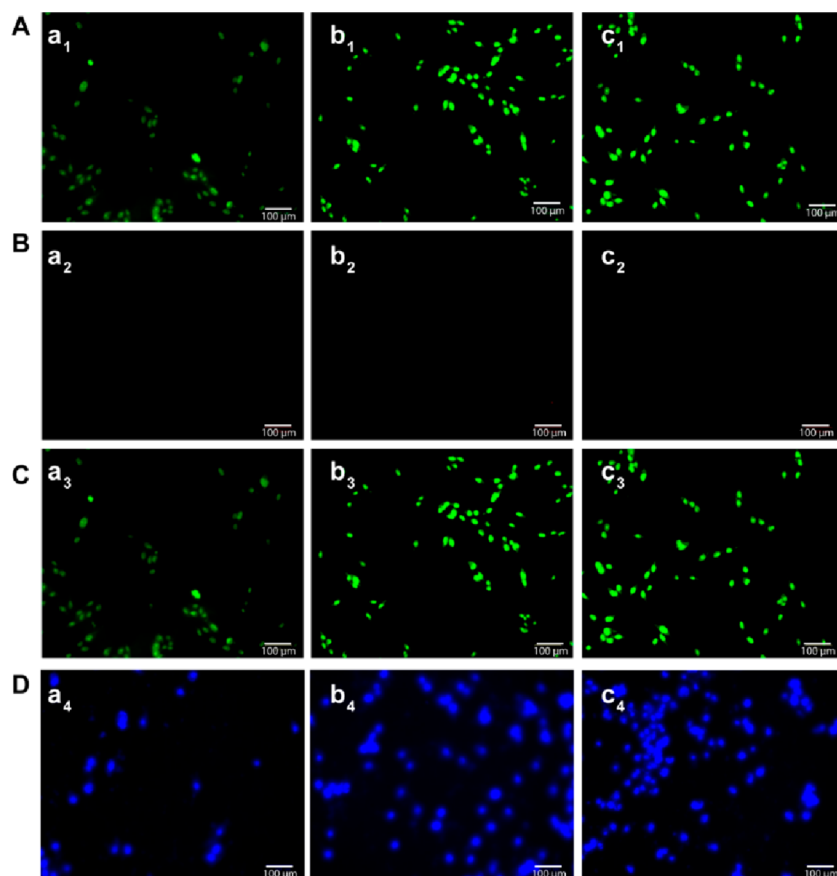


**Figure 10.** Fluorescent micrographs showing AO/EB-stained MG-63 cells with microspheres. (A) Green channel images for (a<sub>1</sub>) alginate, (b<sub>1</sub>) alginate–MoS<sub>2</sub>-1, and (c<sub>1</sub>) alginate–MoS<sub>2</sub>-2; (B) Red channel images for (a<sub>2</sub>) alginate, (b<sub>2</sub>) alginate–MoS<sub>2</sub>-1, and (c<sub>2</sub>) alginate–MoS<sub>2</sub>-2; (C) Merged images of green and red channels for (a<sub>3</sub>) alginate, (b<sub>3</sub>) alginate–MoS<sub>2</sub>-1, and (c<sub>3</sub>) alginate–MoS<sub>2</sub>-2; (D) Hoechst 33342 staining images for (a<sub>4</sub>) alginate, (b<sub>4</sub>) alginate–MoS<sub>2</sub>-1, and (c<sub>4</sub>) alginate–MoS<sub>2</sub>-2. Scale bar = 100  $\mu$ m.

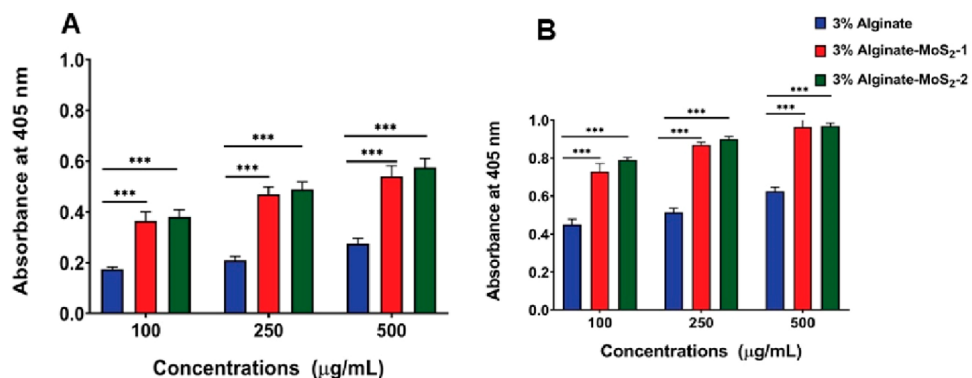


**Figure 11.** Alkaline phosphatase (ALP) activity of alginate, alginate–MoS<sub>2</sub>-1, and alginate–MoS<sub>2</sub>-2 microspheres. ALP activity of the microspheres after (A) 7 days and (B) 14 days of incubation. The data are presented as the mean  $\pm$  standard deviation ( $n = 3$ ), \*  $p < 0.05$ , \*\*  $p < 0.01$ , \*\*\*  $p < 0.001$ ; ns, not significant (compared with 3% alginate microspheres).

MoS<sub>2</sub>-2 microspheres (Figure 8,I). The Ca to P ratios of alginate–MoS<sub>2</sub>-1 and alginate–MoS<sub>2</sub>-2 microspheres were 2.75 and 1.78, respectively. Therefore, these findings revealed that exfoliated nano-MoS<sub>2</sub> could induce mineralization.<sup>79</sup>

**Biocompatibility of the Developed Microspheres with MG-63 Cell Lines.** Evaluating the cytotoxicity of the nanomaterial is critical in measuring its possible biological impact. Several reports showed that nano-MoS<sub>2</sub> was biocompatible with several cell lines. Xu et al. developed exfoliated nano-MoS<sub>2</sub> by using wool keratin. Further, biological assays were

performed using mouse osteoblast cells. The biocompatibility of MoS<sub>2</sub> indicated that it was not toxic to the cells and promoted cell proliferation.<sup>80</sup> In the present study, the developed casein-mediated exfoliated nano-MoS<sub>2</sub> did not show cytotoxicity against the C2C12, MC3T3-E1, and MG-63 cells (Figures 9A–C)). Further, the cytocompatibility of the produced microspheres at various concentrations was determined using the MTT assay (Figure 7C). All cells retained their viability, and all three microsphere samples were nontoxic to the tested cells.<sup>81,82</sup>

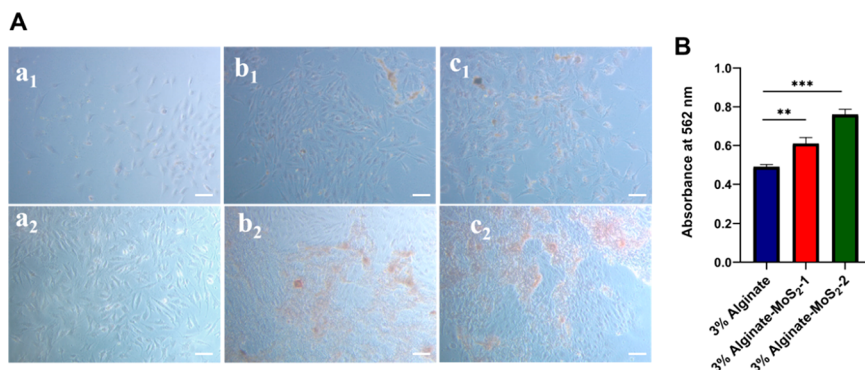


**Figure 12.** Mineralization potential of the developed microspheres on the MG-63 cell lines. In image A, images ( $a_1$ ,  $b_1$ , and  $c_1$ ) are the optical microscopic images of alginate, alginate–MoS<sub>2</sub>-1, and alginate–MoS<sub>2</sub>-2, respectively, taken after 7 days, and images ( $a_2$ ,  $b_2$ ,  $c_2$ ) after 14 days (scale bar = 50  $\mu$ m). Image B represents the quantitative mineralization measured at 562 nm after 14 days. The data are presented as the mean  $\pm$  standard deviation ( $n = 3$ ).

The AO/EB double-staining assay was performed to assess the cell viability of the MG-63 cells with the developed microspheres (Figure 10). Green fluorescence indicates viable cells, and red fluorescence in the nuclei indicates dead cells.<sup>83,84</sup> The results confirmed that the developed microspheres were highly nontoxic to the cells. In addition, the microspheres containing alginate–MoS<sub>2</sub>-1 and alginate–MoS<sub>2</sub>-2 showed higher cell proliferation at higher concentrations. Therefore, the developed alginate–MoS<sub>2</sub>-1 and alginate–MoS<sub>2</sub>-2 microspheres were suitable for bone tissue engineering applications. MG-63 cell attachment and proliferation with the microspheres were further confirmed by Hoechst 33342 staining, which demonstrated that the cells were viable with an intact nucleus in all three microspheres (Figure 10D).

**Alkaline Phosphatase (ALP) and Mineralization Activity.** The ALP activity of the alginate–MoS<sub>2</sub> microspheres after 7 and 14 days is depicted in Figure 11A,B, respectively. Compared to the 3% alginate microspheres, alginate–MoS<sub>2</sub>-1, and alginate–MoS<sub>2</sub>-2 exhibited enhanced ALP activity, which might be due to MoS<sub>2</sub> nanosheets.

Awasthi et al. reported that nanofibers prepared from albumin-exfoliated MoS<sub>2</sub>, zein, and polycaprolactone promoted the ALP activity.<sup>13</sup> Luo et al. developed nanofibers from polyacrylonitrile and MoS<sub>2</sub> and observed enhanced ALP activity with bone marrow mesenchymal stem cells. Upon increasing the concentration of MoS<sub>2</sub> in the nanofibers, the ALP activity improved steadily.<sup>64,85</sup>

Mineralization induced by the alginate, alginate–MoS<sub>2</sub>-1, and alginate–MoS<sub>2</sub>-2 microspheres with the MG-63 cell lines is shown in Figure 12. Alginate microspheres did not produce minerals on day 7 and day 14 (Figure 12,  $a_1$  and  $a_2$ ), whereas better mineralization was observed in the alginate–MoS<sub>2</sub> treated group (Figure 12,  $b_1$ ,  $c_1$ ,  $b_2$ , and  $c_2$ ). Overall, the microspheres containing alginate–MoS<sub>2</sub>-1 and alginate–MoS<sub>2</sub>-2 demonstrated better mineral formation nodules than the microspheres of 3% alginate.

Zhang et al. used the hydrothermal technique to develop nano-MoS<sub>2</sub>. The nano-MoS<sub>2</sub> depicted more effective mineralization when *in vitro* biological experiments were performed on the mesenchymal cells to check their osteogenic capabilities.<sup>86</sup> Awasthi et al. developed nanofibers containing exfoliated nano-MoS<sub>2</sub>, polycaprolactone, and zein. Alizarin Red S test confirmed the mineral deposition on the developed nanofibers.<sup>13</sup> The mineral formation on the nanofibers was due to the presence of nano-MoS<sub>2</sub>. Luo et al. developed MoS<sub>2</sub> and

polycaprolactone-containing nanofiber scaffolding systems. Biological assays demonstrated that the designed scaffold promoted bone marrow-derived mesenchymal stem cell proliferation, and excellent mineral deposition was observed.<sup>85</sup>

## CONCLUSION

The liquid exfoliation method was used to develop MoS<sub>2</sub> nanosheets with casein for biomedical applications. The exfoliated casein–MoS<sub>2</sub> nanosheets were highly stable and cytocompatible. UV-visible spectroscopy confirmed the formation of exfoliated nano-MoS<sub>2</sub>, which exhibited maximum absorption peaks at 610 and 668 nm. Further, FT-IR analysis revealed the functional groups present in casein and exfoliated nano-MoS<sub>2</sub>. Dynamic light scattering analysis, transmission electron microscopy, and atomic force microscopy results confirmed the diameter of the developed materials in the nanometer range. X-ray photoelectron spectroscopy analysis confirmed the presence of Mo and S elements in the exfoliated nano-MoS<sub>2</sub>. Further, alginate was combined with casein–MoS<sub>2</sub> microspheres of different sizes. The developed microspheres were  $1 \pm 0.2$  mm in size. FT-IR analysis confirmed the functional groups present in the microspheres, and XRD analysis revealed the existence of nano-MoS<sub>2</sub> in the microspheres. Further, TGA analysis showed that the inclusion of the nano-MoS<sub>2</sub> in sodium alginate enhanced thermal stability. Besides, increased sustainable degradation and high protein adsorption were observed in the alginate–MoS<sub>2</sub> microspheres compared to alginate microspheres. In addition, excellent apatite formation was observed in the MoS<sub>2</sub> composite scaffold. The alginate–nano-MoS<sub>2</sub> microspheres exhibited good compatibility, improved ALP activity, and enhanced mineralization ability with MG-63 cells. Hence, the developed alginate–nano-MoS<sub>2</sub> microspheres are a promising biomaterial candidate for bone grafting.

## ASSOCIATED CONTENT

### Supporting Information

The Supporting Information is available free of charge at <https://pubs.acs.org/doi/10.1021/acsomega.2c00995>.

Chemical characterization results of nano-MoS<sub>2</sub>-1 and stability of nano-MoS<sub>2</sub>-2 (PDF)

## AUTHOR INFORMATION

### Corresponding Author

Jayachandran Venkatesan – Biomaterials Research Laboratory, Yenepoya Research Centre, Yenepoya (Deemed to be University), Mangalore 575018, India;  orcid.org/0000-0003-1716-8873; Email: venkatjchem@gmail.com

### Authors

Pandurang Appana Dalavi – Biomaterials Research Laboratory, Yenepoya Research Centre, Yenepoya (Deemed to be University), Mangalore 575018, India  
Ashwini Prabhu – Biomaterials Research Laboratory, Yenepoya Research Centre, Yenepoya (Deemed to be University), Mangalore 575018, India  
Sajida M – Biomaterials Research Laboratory, Yenepoya Research Centre, Yenepoya (Deemed to be University), Mangalore 575018, India  
Kaushik Chatterjee – Department of Materials Engineering, Indian Institute of Science, Bangalore 560012, India;  orcid.org/0000-0002-7204-2926

Complete contact information is available at:  
<https://pubs.acs.org/10.1021/acsomega.2c00995>

### Notes

The authors declare no competing financial interest.

## ACKNOWLEDGMENTS

This work was funded by the Indian Council of Medical Research (ICMR), New Delhi (Grant No. 45/27/2020-Nan/BMS), Department of Science and Technology (DST), Government of India (DST/NM/NB/2018/119(G)), and Department of Science and Technology, SERB-TAR/2018/001196. We acknowledge DST-SAIF, Kochi, for providing the support to perform the characterization of the samples. In addition, the authors acknowledge Yenepoya Dental College for providing the Universal Testing Machine to measure the mechanical strength of the composites.

## REFERENCES

- (1) Amini, A. R.; Laurencin, C. T.; Nukavarapu, S. P. Bone tissue engineering: recent advances and challenges. *Crit. Rev. Biomed. Eng.* **2012**, *40* (5), 363–408.
- (2) Tonello, S.; Bianchetti, A.; Braga, S.; Almici, C.; Marini, M.; Piovani, G.; Guindani, M.; Dey, K.; Sartore, L.; Re, F. Impedance-based monitoring of mesenchymal stromal cell three-dimensional proliferation using aerosol jet printed sensors: A tissue engineering application. *Materials* **2020**, *13* (10), 2231.
- (3) Abou Neel, E. A.; Chrzanowski, W.; Salih, V. M.; Kim, H.-W.; Knowles, J. C. Tissue engineering in dentistry. *J. Dent.* **2014**, *42* (8), 915–928.
- (4) Shafiee, A.; Atala, A. Tissue engineering: toward a new era of medicine. *Annu. Rev. Med.* **2017**, *68*, 29–40.
- (5) Koons, G. L.; Diba, M.; Mikos, A. G. Materials design for bone-tissue engineering. *Nat. Rev. Mater.* **2020**, *5* (8), 584–603.
- (6) Kashte, S.; Jaiswal, A. K.; Kadam, S. Artificial bone via bone tissue engineering: current scenario and challenges. *Tissue Eng. Regen. Med.* **2017**, *14* (1), 1–14.
- (7) Scott, T. G.; Blackburn, G.; Ashley, M.; Bayer, I. S.; Ghosh, A.; Biris, A. S.; Biswas, A. Advances in bionanomaterials for bone tissue engineering. *J. Nanosci. Nanotechnol.* **2013**, *13* (1), 1–22.
- (8) Yin, W.; Yu, J.; Lv, F.; Yan, L.; Zheng, L. R.; Gu, Z.; Zhao, Y. Functionalized nano-MoS<sub>2</sub> with peroxidase catalytic and near-infrared photothermal activities for safe and synergistic wound antibacterial applications. *ACS Nano* **2016**, *10* (12), 11000–11011.
- (9) An, S.-J.; Kim, Y. H.; Lee, C.; Park, D. Y.; Jeong, M. S. Exfoliation of transition metal dichalcogenides by a high-power femtosecond laser. *Sci. Rep.* **2018**, *8* (1), 12957.
- (10) Zhu, S.; Gong, L.; Xie, J.; Gu, Z.; Zhao, Y. Design, synthesis, and surface modification of materials based on transition-metal dichalcogenides for biomedical applications. *Small Methods* **2017**, *1* (12), 1700220.
- (11) Dong, R.; Kuljanishvili, I. Progress in fabrication of transition metal dichalcogenides heterostructure systems. *J. Vac. Sci. Technol. B* **2017**, *35* (3), 030803.
- (12) Kasinathan, K.; Murugesan, B.; Pandian, N.; Mahalingam, S.; Selvaraj, B.; Marimuthu, K. Synthesis of biogenic chitosan-functionalized 2D layered MoS<sub>2</sub> hybrid nanocomposite and its performance in pharmaceutical applications: In-vitro antibacterial and anticancer activity. *Int. J. Biol. Macromol.* **2020**, *149*, 1019–1033.
- (13) Awasthi, G. P.; Kaliannagounder, V. K.; Maharjan, B.; Lee, J. Y.; Park, C. H.; Kim, C. S. Albumin-induced exfoliation of molybdenum disulfide nanosheets incorporated polycaprolactone/zein composite nanofibers for bone tissue regeneration. *Mater. Sci. Eng., C* **2020**, *116*, 111162.
- (14) Winchester, A.; Ghosh, S.; Feng, S.; Elias, A. L.; Mallouk, T.; Terrones, M.; Talapatra, S. Electrochemical characterization of liquid phase exfoliated two-dimensional layers of molybdenum disulfide. *ACS Appl. Mater. Interfaces* **2014**, *6* (3), 2125–2130.
- (15) Lv, R.; Robinson, J. A.; Schaak, R. E.; Sun, D.; Sun, Y.; Mallouk, T. E.; Terrones, M. Transition metal dichalcogenides and beyond: Synthesis, properties, and applications of single- and few-layer nanosheets. *Acc. Chem. Res.* **2015**, *48* (1), 56–64.
- (16) Guan, G.; Zhang, S.; Liu, S.; Cai, Y.; Low, M.; Teng, C. P.; Phang, I. Y.; Cheng, Y.; Duei, K. L.; Srinivasan, B. M. Protein induces layer-by-layer exfoliation of transition metal dichalcogenides. *J. Am. Chem. Soc.* **2015**, *137* (19), 6152–6155.
- (17) Coleman, J. N.; Lotya, M.; O'Neill, A.; Bergin, S. D.; King, P. J.; Khan, U.; Young, K.; Gaucher, A.; De, S.; Smith, R. J. Two-dimensional nanosheets produced by liquid exfoliation of layered materials. *Science* **2011**, *331* (6017), 568–571.
- (18) Shortt, J.; Hsu, A. K.; Martin, B. P.; Doggett, K.; Matthews, G. M.; Doyle, M. A.; Ellul, J.; Jockel, T. E.; Andrews, D. M.; Hogg, S. J. The drug vehicle and solvent N-methylpyrrolidone is an immuno-modulator and antimyeloma compound. *Cell Rep.* **2014**, *7* (4), 1009–1019.
- (19) Agarwal, V.; Varghese, N.; Dasgupta, S.; Sood, A.; Chatterjee, K. Engineering a 3D MoS<sub>2</sub> foam using keratin exfoliated nanosheets. *Chem. Eng. J.* **2019**, *374*, 254–262.
- (20) Yadav, U.; Mishra, H.; Singh, V.; Kashyap, S.; Srivastava, A.; Yadav, S.; Saxena, P. S. Enhanced osteogenesis by molybdenum disulfide nanosheet reinforced hydroxyapatite nanocomposite scaffolds. *ACS Biomater. Sci. Eng.* **2019**, *5* (9), 4511–4521.
- (21) Kumar, B. S.; Hemalatha, T.; Deepachitra, R.; Raghavan, R. N.; Prabu, P.; Sastry, T. Biphasic calcium phosphate–casein bone graft fortified with Cassia occidentalis for bone tissue engineering and regeneration. *Bull. Mater. Sci.* **2015**, *38* (1), 259–266.
- (22) Nazari, H.; Heirani-Tabasi, A.; Hajjabbas, M.; Salimi Bani, M.; Nazari, M.; Pirhajati Mahabadi, V.; Rad, I.; Kehtari, M.; Ahmadi Tafti, S. H.; Soleimani, M. Incorporation of SPION-casein core-shells into silk-fibroin nanofibers for cardiac tissue engineering. *J. Cell. Biochem.* **2020**, *121* (4), 2981–2993.
- (23) Abu Diak, O.; Bani-Jaber, A.; Amro, B.; Jones, D.; Andrews, G.P. The manufacture and characterization of casein films as novel tablet coatings. *Food Bioprod. Process.* **2007**, *85* (3), 284–290.
- (24) Kumar, B. S.; Muthukumar, T.; Deepachitra, R.; Charumathy, R.; Hemalatha, T.; Sastry, T. In-vitro evaluation of biphasic calcium phosphate/casein incorporated with Myristica fragrans for bone tissue engineering. *Ceram. Int.* **2015**, *41* (1), 1725–1734.
- (25) Li, Y.; Li, X.; Cao, Z.; Xu, Y.; Gong, Y.; Shi, X. Fabrication of uniform casein/CaCO<sub>3</sub> vaterite microspheres and investigation of its formation mechanism. *Cryst. Growth Des.* **2017**, *17* (12), 6178–6188.

- (26) Li, Z.; Ramay, H. R.; Hauch, K. D.; Xiao, D.; Zhang, M. Chitosan–alginate hybrid scaffolds for bone tissue engineering. *Biomaterials* **2005**, *26* (18), 3919–3928.
- (27) Luo, Y.; Wu, C.; Lode, A.; Gelinsky, M. Hierarchical mesoporous bioactive glass/alginate composite scaffolds fabricated by three-dimensional plotting for bone tissue engineering. *Biofabrication* **2013**, *5* (1), 015005.
- (28) Sharma, C.; Dinda, A. K.; Potdar, P. D.; Chou, C.-F.; Mishra, N. C. Fabrication and characterization of novel nano-biocomposite scaffold of chitosan–gelatin–alginate–hydroxyapatite for bone tissue engineering. *Mater. Sci. Eng., C* **2016**, *64*, 416–427.
- (29) Hernández-González, A. C.; Téllez-Jurado, L.; Rodríguez-Lorenzo, L. M. Alginate hydrogels for bone tissue engineering, from injectables to bioprinting: A review. *Carbohydr. Polym.* **2020**, *229*, 115514.
- (30) Wee, C. Y.; Yang, Z.; Thian, E. S. Past, present and future development of microspheres for bone tissue regeneration: a review. *Mater. Technol.* **2021**, *36* (6), 364–374.
- (31) Huang, W.; Li, X.; Shi, X.; Lai, C. Microsphere based scaffolds for bone regenerative applications. *Biomater. Sci.* **2014**, *2* (9), 1145–1153.
- (32) G.V, Y. D.; Prabhu, A.; Anil, S.; Venkatesan, J. Preparation and characterization of dexamethasone loaded sodium alginate-graphene oxide microspheres for bone tissue engineering. *J. Drug Delivery Sci. Technol.* **2021**, *64*, 102624.
- (33) Fabbri, P.; Bondioli, F.; Messori, M.; Bartoli, C.; Dinucci, D.; Chiellini, F. Porous scaffolds of polycaprolactone reinforced with in situ generated hydroxyapatite for bone tissue engineering. *J. Mater. Sci. Mater. Med.* **2010**, *21* (1), 343–351.
- (34) Olad, A.; Hagh, H. B. K.; Mirmohseni, A.; Azhar, F. F. Graphene oxide and montmorillonite enriched natural polymeric scaffold for bone tissue engineering. *Ceram. Int.* **2019**, *45* (12), 15609–15619.
- (35) Kavya, K. C.; Jayakumar, R.; Nair, S.; Chennazhi, K. P. Fabrication and characterization of chitosan/gelatin/nSiO<sub>2</sub> composite scaffold for bone tissue engineering. *Int. J. Biol. Macromol.* **2013**, *59*, 255–263.
- (36) Tohamy, K. M.; Mabrouk, M.; Soliman, I. E.; Beherei, H. H.; Aboelnasr, M. A. Novel alginate/hydroxyethyl cellulose/hydroxyapatite composite scaffold for bone regeneration: In vitro cell viability and proliferation of human mesenchymal stem cells. *Int. J. Biol. Macromol.* **2018**, *112*, 448–460.
- (37) Purohit, S. D.; Bhaskar, R.; Singh, H.; Yadav, I.; Gupta, M. K.; Mishra, N. C. Development of a nanocomposite scaffold of gelatin–alginate–graphene oxide for bone tissue engineering. *Int. J. Biol. Macromol.* **2019**, *133*, 592–602.
- (38) Kokubo, T.; Takadama, H. How useful is SBF in predicting in vivo bone bioactivity? *Biomaterials* **2006**, *27* (15), 2907–2915.
- (39) Cho, Y. S.; Jung, W. K.; Kim, J. A.; Choi, I. W.; Kim, S. K. Beneficial effects of fucoidan on osteoblastic MG-63 cell differentiation. *Food Chem.* **2009**, *116* (4), 990–994.
- (40) Dalavi, P. A.; Prabhu, A.; Shastry, R. P.; Venkatesan, J. Microspheres containing biosynthesized silver nanoparticles with alginate-nano hydroxyapatite for biomedical applications. *J. Biomater. Sci., Polym. Ed.* **2020**, *31* (16), 2025–2043.
- (41) Venkatesan, J.; Bhatnagar, I.; Kim, S.-K. Chitosan-alginate biocomposite containing fucoidan for bone tissue engineering. *Mar. Drugs* **2014**, *12* (1), 300–316.
- (42) Wang, D.; Song, L.; Zhou, K.; Yu, X.; Hu, Y.; Wang, J. Anomalous nano-barrier effects of ultrathin molybdenum disulfide nanosheets for improving the flame retardance of polymer nanocomposites. *J. Mater. Chem. A* **2015**, *3* (27), 14307–14317.
- (43) Dolai, S.; Maiti, P.; Ghorai, A.; Bhunia, R.; Paul, P. K.; Ghosh, D. Exfoliated molybdenum disulfide-wrapped CdS nanoparticles as a nano-heterojunction for photo-electrochemical water splitting. *ACS Appl. Mater. Interfaces* **2021**, *13* (1), 438–448.
- (44) Ptíček Siročić, A.; Kratofil Krehula, L.; Katančić, Z.; Hrnjak-Murgić, Z. Characterization of casein fractions—Comparison of commercial casein and casein extracted from cow's milk. *Chem. Biochem. Eng. Q.* **2017**, *30* (4), 501–509.
- (45) Wang, D.; Zhou, K.; Yang, W.; Xing, W.; Hu, Y.; Gong, X. Surface modification of graphene with layered molybdenum disulfide and their synergistic reinforcement on reducing fire hazards of epoxy resins. *Ind. Eng. Chem. Res.* **2013**, *52* (50), 17882–17890.
- (46) Rahmati, B.; Sarhan, A. A.; Sayuti, M. Morphology of surface generated by end milling AL6061-T6 using molybdenum disulfide (MoS<sub>2</sub>) nanolubrication in end milling machining. *J. Clean. Prod.* **2014**, *66*, 685–691.
- (47) Shakya, J.; Kumar, S.; Kanjilal, D.; Mohanty, T. Work function modulation of molybdenum disulfide nanosheets by introducing systematic lattice strain. *Sci. Rep.* **2017**, *7* (1), 1–9.
- (48) Yan, R.; Simpson, J. R.; Bertolazzi, S.; Brivio, J.; Watson, M.; Wu, X.; Kis, A.; Luo, T.; Hight Walker, A. R.; Xing, H. G. Thermal conductivity of monolayer molybdenum disulfide obtained from temperature-dependent Raman spectroscopy. *ACS Nano* **2014**, *8* (1), 986–993.
- (49) Sim, H.; Lee, J.; Park, B.; Kim, S. J.; Kang, S.; Ryu, W.; Jun, S. C. High-concentration dispersions of exfoliated MoS<sub>2</sub> sheets stabilized by freeze-dried silk fibroin powder. *Nano Res.* **2016**, *9* (6), 1709–1722.
- (50) Xuan, D.; Zhou, Y.; Nie, W.; Chen, P. Sodium alginate-assisted exfoliation of MoS<sub>2</sub> and its reinforcement in polymer nanocomposites. *Carbohydr. Polym.* **2017**, *155*, 40–48.
- (51) Huang, X.-W.; Wei, J.-J.; Liu, T.; Zhang, X.-L.; Bai, S.-M.; Yang, H.-H. Silk fibroin-assisted exfoliation and functionalization of transition metal dichalcogenide nanosheets for antibacterial wound dressings. *Nanoscale* **2017**, *9* (44), 17193–17198.
- (52) Konarova, M.; Tang, F.; Chen, J.; Wang, G.; Rudolph, V.; Beltramini, J. Nano-and microscale engineering of the molybdenum disulfide-based catalysts for syngas to ethanol conversion. *Chem-CatChem.* **2014**, *6* (8), 2394–2402.
- (53) Li, Y.; Zheng, Z.; Cao, Z.; Zhuang, L.; Xu, Y.; Liu, X.; Xu, Y.; Gong, Y. Enhancing proliferation and osteogenic differentiation of HMSCs on casein/chitosan multilayer films. *Colloids Surf., B* **2016**, *141*, 397–407.
- (54) Qin, L.; Dong, H.; Mu, Z.; Zhang, Y.; Dong, G. Preparation and bioactive properties of chitosan and casein phosphopeptides composite coatings for orthopedic implants. *Carbohydr. Polym.* **2015**, *133*, 236–244.
- (55) Ganta, D.; Sinha, S.; Haasch, R. T. 2-D material molybdenum disulfide analyzed by XPS. *Surf. Sci. Spectra* **2014**, *21* (1), 19–27.
- (56) Zhang, X.; Jia, F.; Yang, B.; Song, S. Oxidation of molybdenum disulfide sheet in water under in situ atomic force microscopy observation. *J. Phys. Chem. C* **2017**, *121* (18), 9938–9943.
- (57) Hu, X.; Hu, S.; Zhao, Y. Synthesis of nanometric molybdenum disulphide particles and evaluation of friction and wear properties. *Lubr. Sci.* **2005**, *17* (3), 295–308.
- (58) Xin, S.; Chimene, D.; Garza, J. E.; Gaharwar, A. K.; Alge, D. L. Clickable PEG hydrogel microspheres as building blocks for 3D bioprinting. *Biomater. Sci.* **2019**, *7* (3), 1179–1187.
- (59) Ochsenbein, A. M.; Karaman, S.; Proulx, S. T.; Goldmann, R.; Chittazhathu, J.; Dasargyri, A.; Chong, C.; Leroux, J.-C.; Stanley, E. R.; Detmar, M. Regulation of lymphangiogenesis in the diaphragm by macrophages and VEGFR-3 signaling. *Angiogenesis* **2016**, *19* (4), S13–S24.
- (60) Fernandes, M.; Gonçalves, I. C.; Nardecchia, S.; Amaral, I. F.; Barbosa, M. A.; Martins, M. C. L. Modulation of stability and mucoadhesive properties of chitosan microspheres for therapeutic gastric application. *Int. J. Pharm.* **2013**, *454* (1), 116–124.
- (61) Torres, M. L.; Fernandez, J.; Dellatorre, F. G.; Cortizo, A. M.; Oberti, T. G. Purification of alginate improves its biocompatibility and eliminates cytotoxicity in matrix for bone tissue engineering. *Algal Res.* **2019**, *40*, 101499.
- (62) Gholizadeh, B. S.; Buazar, F.; Hosseini, S. M.; Mousavi, S. M. Enhanced antibacterial activity, mechanical and physical properties of alginate/hydroxyapatite bionanocomposite film. *Int. J. Biol. Macromol.* **2018**, *116*, 786–792.

- (63) Bindhu, B.; Sharu, B.; Gopika, M.; Praseetha, P.; Veluraja, K. Molybdenum disulfide nanoflakes through Li-AHA assisted exfoliation in an aqueous medium. *Rsc Advances* **2016**, *6* (26), 22026–22033.
- (64) Wu, S.; Wang, J.; Jin, L.; Li, Y.; Wang, Z. Effects of polyacrylonitrile/MoS<sub>2</sub> composite nanofibers on the growth behavior of bone marrow mesenchymal stem cells. *ACS Appl. Nano Mater.* **2018**, *1* (1), 337–343.
- (65) Khaledian, S.; Kahrizi, D.; Balaky, S. T. J.; Arkan, E.; Abdoli, M.; Martinez, F. Electrospun nanofiber patch based on gum tragacanth/polyvinyl alcohol/molybdenum disulfide composite for tetracycline delivery and their inhibitory effect on Gram+ and Gram-bacteria. *J. Mol. Liq.* **2021**, *334*, 115989.
- (66) Dodero, A.; Vicini, S.; Alloisio, M.; Castellano, M. Sodium alginate solutions: correlation between rheological properties and spinnability. *J. Mater. Sci.* **2019**, *S4* (10), 8034–8046.
- (67) Liu, S.; Li, Y.; Li, L. Enhanced stability and mechanical strength of sodium alginate composite films. *Carbohydr. Polym.* **2017**, *160*, 62–70.
- (68) Coradin, T.; Livage, J. Synthesis and characterization of alginate/silica biocomposites. *J. Sol-Gel Sci. Technol.* **2003**, *26* (1), 1165–1168.
- (69) Ionita, M.; Pandele, M. A.; Iovu, H. Sodium alginate/graphene oxide composite films with enhanced thermal and mechanical properties. *Carbohydr. Polym.* **2013**, *94* (1), 339–344.
- (70) Przekora, A.; Palka, K.; Ginalski, G. Biomedical potential of chitosan/HA and chitosan/β-1, 3-glucan/HA biomaterials as scaffolds for bone regeneration—A comparative study. *Mater. Sci. Eng., C* **2016**, *58*, 891–899.
- (71) Thein-Han, W. W.; Misra, R. D. K. Biomimetic chitosan-nanohydroxyapatite composite scaffolds for bone tissue engineering. *Acta Biomater.* **2009**, *5* (4), 1182–1197.
- (72) Abouzeid, R. E.; Khiari, R.; Beneventi, D.; Dufresne, A. Biomimetic mineralization of three-dimensional printed alginate/TEMPO-oxidized cellulose nanofibril scaffolds for bone tissue engineering. *Biomacromolecules* **2018**, *19* (11), 4442–4452.
- (73) Kumar Saini, R.; Prasad Bagri, L.; Bajpai, A.K. Nano-silver hydroxyapatite based antibacterial 3D scaffolds of gelatin/alginate/poly (vinyl alcohol) for bone tissue engineering applications. *Colloids Surf., B* **2019**, *177*, 211–218.
- (74) Dreifke, M. B.; Ebraheim, N. A.; Jayasuriya, A. C. Investigation of potential injectable polymeric biomaterials for bone regeneration. *J. Biomed. Mater. Res.* **2013**, *101* (8), 2436–2447.
- (75) Kouhi, M.; Morshed, M.; Varshosaz, J.; Fathi, M. H. Poly ( $\epsilon$ -caprolactone) incorporated bioactive glass nanoparticles and simvastatin nanocomposite nanofibers: Preparation, characterization and in vitro drug release for bone regeneration applications. *Chem. Eng. J.* **2013**, *228*, 1057–1065.
- (76) Zamani, D.; Moztarzadeh, F.; Bizari, D. Alginate-bioactive glass containing Zn and Mg composite scaffolds for bone tissue engineering. *Int. J. Biol. Macromol.* **2019**, *137*, 1256–1267.
- (77) Chesnutt, B. M.; Viano, A. M.; Yuan, Y.; Yang, Y.; Guda, T.; Appleford, M. R.; Ong, J. L.; Haggard, W. O.; Bumgardner, J. D. Design and characterization of a novel chitosan/nanocrystalline calcium phosphate composite scaffold for bone regeneration. *J. Biomed. Mater. Res.* **2009**, *88* (2), 491–502.
- (78) Gheisari, H.; Karamian, E.; Abdellahi, M. A novel hydroxyapatite–hardystonite nanocomposite ceramic. *Ceram. Int.* **2015**, *41* (4), 5967–5975.
- (79) Li, H.; Jiang, F.; Ye, S.; Wu, Y.; Zhu, K.; Wang, D. Bioactive apatite incorporated alginate microspheres with sustained drug-delivery for bone regeneration application. *Mater. Sci. Eng., C* **2016**, *62*, 779–786.
- (80) Xu, X.; Wu, J.; Meng, Z.; Li, Y.; Huang, Q.; Qi, Y.; Liu, Y.; Zhan, D.; Liu, X. Y. Enhanced exfoliation of biocompatible MoS<sub>2</sub> nanosheets by wool keratin. *ACS Appl. Nano Mater.* **2018**, *1* (10), 5460–5469.
- (81) Cholas, R.; Padmanabhan, S. K.; Gervaso, F.; Udayan, G.; Monaco, G.; Sannino, A.; Licciulli, A. Scaffolds for bone regeneration made of hydroxyapatite microspheres in a collagen matrix. *Mater. Sci. Eng., C* **2016**, *63*, 499–505.
- (82) Khatami, N.; Khoshfetrat, A. B.; Khaksar, M.; Zamani, A. R. N.; Rahbarghazi, R. Collagen-alginate-nano-silica microspheres improved the osteogenic potential of human osteoblast-like MG-63 cells. *J. Cell. Biochem.* **2019**, *120* (9), 15069–15082.
- (83) Zhao, Y.; Fan, T.; Chen, J.; Su, J.; Zhi, X.; Pan, P.; Zou, L.; Zhang, Q. Magnetic bioinspired micro/nanostructured composite scaffold for bone regeneration. *Colloids Surf., B* **2019**, *174*, 70–79.
- (84) Zou, L.; Zhang, Y.; Liu, X.; Chen, J.; Zhang, Q. Biomimetic mineralization on natural and synthetic polymers to prepare hybrid scaffolds for bone tissue engineering. *Colloids Surf., B* **2019**, *178*, 222–229.
- (85) Luo, S.; Wu, S.; Xu, J.; Zhang, X.; Zou, L.; Yao, R.; Jin, L.; Li, Y. Osteogenic differentiation of BMSCs on MoS<sub>2</sub> composite nanofibers with different cell seeding densities. *Appl. Nanosci.* **2020**, *10* (9), 3703–3716.
- (86) Zhang, X.; Nie, J.; Yang, X.; Liu, Z.; Guo, W.; Qiu, J.; Wang, S.; Yu, X.; Guan, Y.; Liu, H. Nanostructured molybdenum disulfide biointerface for adhesion and osteogenic differentiation of mesenchymal stem cells. *Appl. Mater. Today* **2018**, *10*, 164–172.

## □ Recommended by ACS

### BMP2-Mediated Silica Deposition: An Effective Strategy for Bone Mineralization

Mi-Ran Ki, Seung Pil Pack, et al.

JANUARY 28, 2022

ACS BIOMATERIALS SCIENCE & ENGINEERING

READ ▾

### Development and Characterization of a Biocomposite Material from Chitosan and New Zealand-Sourced Bovine-Derived Hydroxyapatite for Bone Regeneration

Jeffrey Huang, George J. Dias, et al.

JULY 01, 2020

ACS OMEGA

READ ▾

### In Situ Bending Reveals Simultaneous Enhancements of Strength and Ductility of Cortical and Cancellous Layers Induced by the Cartilage Layer

Zhichao Ma, Luquan Ren, et al.

NOVEMBER 12, 2021

ACS OMEGA

READ ▾

### Mesoporous Hydroxyapatite Nanoparticles Mediate the Release and Bioactivity of BMP-2 for Enhanced Bone Regeneration

Yubei Qiu, Jiang Chen, et al.

MARCH 18, 2020

ACS BIOMATERIALS SCIENCE & ENGINEERING

READ ▾

Get More Suggestions >